A Combined Experimental and Theoretical Charge Density Study of the Chemical Bonding and Magnetism in 3-Amino-propanolato Cu(II) Complexes Containing Weakly Coordinated Anions

Louis J. Farrugia,*,† Derek S. Middlemiss,† Reijo Sillanpää,‡ and Petri Seppälä‡

WestCHEM, Department of Chemistry, University of Glasgow, Glasgow G12 8QQ Scotland U.K., and Department of Chemistry, P.O. Box 35, FIN-40014, University of Jyväskylä, Jyväskylä, Finland

Received: June 2, 2008; Revised Manuscript Received: July 18, 2008

The experimental (100 K) and theoretical charge densities in the binuclear complexes $[Cu_2(ap)_2(L)_2]$ (ap = 3-aminopropanolate) **1** (L = nitrite), **2** (L = nitrate), and **3** (L = formate) have been examined. These complexes contain the same centrosymmetric alkoxy-bridged motif, where each strongly Jahn−Teller distorted Cu(II) ion is ligated to three O atoms and one N atom in a square-planar arrangement. This primary coordination sphere is augmented by a long contact with the O atom of a pendant L anion from an adjacent molecule in the crystal lattice. Topological analyses of the experimental and theoretical densities according to the quantum theory of atoms in molecules (QTAIM) are in excellent agreement. Consideration of a number of topological indicators including $\rho(\mathbf{r})$, $\nabla^2\rho(\mathbf{r})$, the delocalization indices $\delta(A,B)$, and the integral $\oint_{A\cap B} \rho(\mathbf{r})$ of the density over the zero flux surface shared by the two atoms confirms that the Cu−O and Cu−N bonding in the primary coordination sphere has a strong covalent component, but the weak Cu···O interactions are primarily electrostatic in nature. In this first investigation of the source function in a coordination complex, it is shown to provide an insight into the differing electrostatic and covalent contributions to the chemical bonds. The two Cu(II) centers are strongly antiferromagnetically coupled, but the topological analyses indicates the lack of any direct Cu···Cu interaction. The molecular graph suggests an exchange pathway via the bridging O-atoms, thus providing experimental support of the classical superexchange mechanism. Periodic DFT calculations on **2** and **3** show that the intradimer coupling proceeds via spin-delocalization and provide values of the magnetic coupling constants $-2J$ of 324.5 and 244.8 cm^{-1}, respectively, which compare well with the previously determined experimental values.

Introduction

The magnetic behavior of polynuclear transition metal coordination compounds is a subject of intense interest because of wide-ranging potential applications.[1] One classic series of compounds, which has been intensively investigated over the last few decades, are the hydroxy- and alkoxy-bridged binuclear Cu(II) complexes.[2] Taken together, the single unpaired electron on each Cu(II) center forms a relatively simple magnetic exchange system, and depending on the geometry and nature of the other ancilliary ligands, the two Cu(II) ions may be either ferromagnetically or antiferromagnetically coupled. The magnetostructural correlations of the hydroxy- and alkoxy-bridged Cu(II) dimers were investigated by Hatfield, Hodgson et al.[2a] who established that the primary geometric factor determining the magnitude of the exchange coupling was the Cu−O−Cu angle. Hoffmann and co-workers[3a] rationalized this finding in terms of the variation in the degree of overlap of the in-plane O(*p*)-orbitals, as embodied in the classical superexchange model.[4] A similar interpretation was later advanced by Kahn.[3b] More recent ab initio calculations[5] indicated that, although the Cu−O−Cu angle is the single most important parameter, other geometric factors such as the pyramidality at the bridging O atoms and the tetrahedral distortion at the Cu(II) center also played a significant role in determining the sign and magnitude of the singlet−triplet splitting $-2J$.

The quantum theory of atoms in molecules (QTAIM) of Bader[6] is a powerful method for extracting chemical information from the total charge density, in particular because the approach is equally valid for densities derived from quantum calculations or from experiment by using high-resolution X-ray diffraction data.[7] Indeed, the interplay between theory and experiment[8] in this area has provided a driving force for methodological development. In most cases, the QTAIM allows reconstruction of the chemical structure, solely on the basis of an analysis of the gradient vector field and its associated critical points. A number of experimental QTAIM studies on coordination complexes containing magnetically interacting metal ions have been recently reported,[9] with a view to better understand the coupling mechanisms. Although the electronic charge density cannot be related directly to the spin density, topological analyses may offer some indirect insights into the magnetism of a complex through the resulting network of critical points and associated bond paths.[6] The chemical significance of these paths has been the subject of much recent debate.[10] Partly in answer to the criticisms raised, Pendás et al. recently proposed[11] an interpretation in terms of a privileged pathway of exchange, which means that the bond path network may be used to assess the relative contribution of each exchange bridge.

With a view to examining these issues, we herein present a combined experimental and theoretical charge density study on the closely related series of binuclear Cu(II) coordination

---

* Corresponding author. Fax +441413304888. E-mail: louis@chem.gla.ac.uk.
† University of Glasgow.
‡ University of Jyväskylä.

10.1021/jp804865j CCC: $40.75

TABLE 1: Experimental Details[a]

	compound number			
	1 (APEX II)	**1 (KappaCCD)**	**2**	**3**
compound formula	$C_6H_{16}Cu_2N_4O_6$	$C_6H_{16}Cu_2N_4O_6$	$C_6H_{16}Cu_2N_4O_8$	$C_8H_{18}Cu_2N_2O_6$
compound color	dark blue	dark blue	dark blue	dark blue
M_r	367.31	367.31	399.31	365.32
space group	*Pbca*	*Pbca*	$P2_1/c$	$P2_1/c$
crystal system	orthorhombic	orthorhombic	monoclinic	monoclinic
a	8.3395(3)	8.3459(2)	8.8024(3)	8.4758(3)
b /Å	8.5023(3)	8.5084(2)	8.0562(2)	8.7735(3)
c /Å	17.1507(5)	17.1684(5)	9.2531(3)	8.3445(3)
β /deg	90	90	104.818(1)	99.616(2)
V /Å^{-3}	1216.07(7)	1219.13(5)	634.35(3)	611.80(4)
Z	4	4	2	2
D_{calc} /g cm^{-3}	2.01	2.00	2.09	1.98
$F(000)$	744	744	404	372
λ/Å	0.71073	0.71073	0.71073	0.71073
μ(Mo−K$_a$) /mm^{-1}	3.524	3.515	3.398	3.497
crystal size /mm	0.35 × 0.30 × 0.13	0.42 × 0.40 × 0.12	0.24 × 0.21 × 0.20	0.32 × 0.28 × 0.20
transmission coefficients (range)	0.357−0.640	0.236−0.663	0.433−0.607	0.404−0.549
θ range /deg	3.41−59.0	3.40−52.2	2.39−60.04	2.44−54.16
no. of data used for merging	227269	210269	112898	157082
No. of unique data	8930	6973	9485	7570
hkl range	−19→20; −20→20; −40→41	−18→18; −18→18; −37→37	−21→21; −19→15; −21→22	−19→19; −19→18; −18→18
R_{int}	0.0421	0.0302	0.0357	0.0369
R_σ	0.0303	0.0264	0.0311	0.0271
Spherical Atom Refinement				
no. of data in refinement	8930	6973	9485	7570
no. of refined parameters	82	83	100	119
final R [$I > 2\sigma(I)$] (all data)	0.0251(0.0355)	0.0233 (0.0296)	0.020 (0.0297)	0.016 (0.0212)
R_w^2 [$I > 2\sigma(I)$] (all data)	0.0620 (0.0641)	0.0553 (0.0573)	0.0496 (0.0515)	0.0421 (0.0431)
goodness of fit S	1.096	1.174	1.024	1.062
residuals in electron density map /eÅ^{-3}	1.154 (max), −1.18 (min)	0.983 (max), −0.803 (min)	1.187 (max), −0.693 (min)	0.688 (max) −0.904 (min)
Max shift /esd. in last cycle	0.007	0.002	$<10^{-3}$	$<10^{-3}$
Multipole Refinement				
no. of data in refinement	7302	6120	7905	6732
no. of refined parameters (last cycle)	275	274	299	279
final R [$F > 4\sigma(F)$] (all data)	0.021(0.038)	0.020(0.026)	0.017(0.032)	0.013(0.021)
R_w[$F > 4\sigma(F)$]	0.029	0.028	0.018	0.017
goodness of fit S	1.618	1.692	0.977	1.047
electron density residuals (all data) /eÅ^{-3}	1.069, −0.820 0.101 (rms)	0.941, −0.636 0.095 (rms)	0.687, −0.340 0.068 (rms)	0.702, −0.339; 0.057 (rms)
(truncated data, (sin θ)/λ ≤ 0.8 Å^{-1}) /eÅ^{-3}	0.436, −0.513 0.060 (rms)	0.308, −0.215 0.095 (rms)	0.254, −0.206 0.036 (rms)	0.258, −0.165; 0.036 (rms)
max shift /esd. in last cycle	$<10^{-3}$	$<10^{-3}$	$<10^{-3}$	$<10^{-3}$

[a] $R = \sum (|F_o| - |F_c|)/\sum (F_o)$; $R_w = \{\sum(w(F_o - F_c)^2)/\sum(w(F_o)^2)\}^{1/2}$; $R_{int} = \sum \{n/(n-1)\}^{1/2} \mid F_o^2 - F_o^2(\text{mean})\mid/\sum F_o^2$ (summation is carried out only where more than one symmetry equivalent is averaged); $R_w^2 = \{\sum(w(F_o^2 - F_c^2)^2)/\sum(w(F_o^2)^2)\}^{1/2}$; $R_\sigma = \sum [\sigma(F_o^2)]/\sum [F_o^2]$.

complexes [$Cu_2(ap)_2(L)_2$] (ap = 3-aminopropanolate) **1** (L = nitrite), **2** (L = nitrate), and **3** (L = formate), originally reported by Sillanpää et al.[12] Magnetic susceptibility measurements on these complexes,[12a,13] modeled by using the Bleaney−Bowers[14] equation, showed that the two Cu(II) centers within the dimer are strongly antiferromagnetically coupled, with $-2J$ values of 300, 387, and 282 cm^{-1}, respectively. As discussed below, these complexes are polymerized in the solid state through weak interactions between the strongly Jahn−Teller distorted Cu(II) ions and the L$^-$ anions from adjacent complexes. Lecomte and co-workers have recently reported an in-depth study[9a] on a related layered antiferromagnetic Cu(II) compound $Cu_2(OH)_3NO_3$. A few other topological charge density studies on Cu(II) complexes have appeared,[15] including a number of earlier investigations[16] performed by using deformation density analysis. For complex **1**, we present analyses based on two data sets collected on different diffractometers with different crystal specimens, allowing an assessment of the effect of experimental data on the variability of the derived density.

Experimental Procedures

Preparation of [$Cu_2(ap)_2(NO_2)_2$]. A total of 0.24 mmol of $NaNO_2$ was dissolved in 90 mL of MeOH. To this solution was added 0.2 mmol of $Cu(ClO_4)_2 \cdot 6H_2O$ and 0.48 mmol of 3-amino-1-propanol (Hap) in 10 mL of MeOH. The blue solution was allowed to stand at room temperature for a week. The blue crystals (22% yield) of compound **1** were filtered and washed with ethanol and diethyl ether. Compounds **2** and **3** were prepared by the literature methods.[12] Crystals of **1**−**3**, with well-formed morphologies suitable for charge density studies, were obtained by recrystallization from methanol.

Data Collection, Processing, and Spherical Atom Refinement. Details of data collection procedures are given in Table 1. Single crystals of suitable size were attached to a glass fiber by using silicone grease and mounted on a goniometer head in a general position. They were cooled from ambient temperature to 100 K over a period of 1 h by using an Oxford Instruments N-Helix with nitrogen gas as coolant. Data were collected by using ω- and φ-oscillation scans of 0.5° on a Bruker Kappa APEX II diffractometer, equipped with a kappa-geometry goniostat, and running under APEX2 software.[17] In the following descriptions, numerical data are given for complex **1**, with the corresponding values for **2** and **3**, respectively, in parentheses. A total of 14270 (12907, 16401) images in 36 (32, 48) scan sets were measured over a time period of 68.6 (72.3, 74.9) h. The images were integrated, and precise unit cell dimensions and errors were determined by postrefinement of the setting angles of the reflections by using the SAINT integration software.[17] Absorption corrections by Gaussian quadrature,[18] based on the measured crystal faces, were applied to the reflection data. The data were then scaled, and a semiempirical correction[19] (without a theta-dependent correction) was applied by using the program SADABS[20] to remove any residual absorption anisotropy due to the mounting medium and to account for other instrumental instabilities. Typical correction factors were in the range 0.7–0.9. A total of 227269 (112898, 157082) intensity measurements remained after removal of systematic absences. These were then sorted and merged by using SORTAV,[21] giving 8931 (9485, 7570) unique independent data with a mean redundancy of 25.4 (11.6, 20.8). A spherical atom refinement performed by using SHELXL97-2[22] was initially undertaken, with full-matrix least-squares on F^2 and by using all the unique data. All non-H atoms were allowed anisotropic thermal motion. Neutral atom scattering factors, coefficients of anomalous dispersion, and absorption coefficients were obtained from ref 23. Details of this refinement are given in Table 1. Thermal ellipsoid plots were obtained by using the program ORTEP-3 for Windows.[24] All calculations were carried out by using the WinGX package[25] of crystallographic programs. For complex **1**, a second data set with slightly lower resolution was obtained on a Bruker-Nonius KappaCCD diffractometer. The data were integrated and processed as previously described[26] by using Denzo.[27] The integrated data were then processed as described above by using a numerical absorption correction based on the crystal faces, followed by scaling by using SADABS[20] and merging by using SORTAV.[21] All data sets are 100% complete to a resolution limit of $(\sin\theta)/\lambda \le 1.1$ Å^{-1}.

Multipole Refinement. The multipole formalism of Hansen and Coppens[28] as implemented in the XD-2006 program suite[29a] was used. The aspherical atomic electron density $\rho(\mathbf{r})$ is given by

$$\rho(\mathbf{r}) = \rho_c(\mathbf{r}) + P_v\kappa^3\rho_v(\kappa\mathbf{r}) + \rho_d(\kappa'\mathbf{r}) \qquad (1)$$

where ρ_c and ρ_v are respectively the core and spherical valence densities and

$$\rho_d(\kappa'\mathbf{r}) = \sum_{l=0}\kappa^3 R_l(\kappa'\mathbf{r})\sum_{m=0}^{l} P_{lm\pm}y_{lm\pm}(\mathbf{r}/r) \qquad (2)$$

is the term accounting for the deformation valence densities. The $y_{lm\pm}$ are density-normalized, real spherical harmonics and P_v and $P_{lm\pm}$ are the refinable populations. The function minimized in the least-squares procedure was $\Sigma w(|F_o| - k|F_c|)^2$, with only those reflections with $F > 4\sigma(F)$ included in the refinement, with weights w taken as $1/\sigma^2(F)$. The multipole expansion was truncated at the hexadecapole level for the Cu atoms, at the octupole level for the O, N, and C atoms, and at the quadrupole level for the H atoms. The hydrogen positional parameters were fixed at the neutron determined distances of 1.083 Å for the methylene groups, 1.0 Å for the N–H atoms and 1.07 Å for the formate C–H atom. The importance of utilizing anisotropic displacement parameters (adp's) for the H atoms in multipole refinements has recently been stressed.[30] In the absence of neutron diffraction data, the H-atom adp's were estimated by using the method described by Madsen.[31] This procedure approximates the H atom adp's as a convolution of the non-H atom rigid-body thermal motion with internal mean-square displacements for the H-atoms obtained from a database. The H-atom adp's used in this study were obtained by using the SHADE web-server[31b] and were subsequently kept fixed in all refinements. For all complexes, this method of predicting the H-atom adp's gave a small improvement in residuals over models using the standard isotropic approximation and therefore was considered a satisfactory approximation. Isosurface plots were obtained by using the MOLISO program,[29b] and the exact experimental electrostatic potentials[29c] were calculated by using the EP/MM method[29d] as implemented in XD-2006.[29a]

Each pseudoatom was assigned a neutral atom core and spherical-valence scattering factor derived from the relativistic Dirac–Fock wave functions of Su and Coppens[32] expanded in terms of the single-ζ functions of Bunge, Barrientos, and Bunge.[33] The valence deformation functions for all atoms apart from Cu used a single-ζ Slater-type radial function multiplied by the density-normalized spherical harmonics. The radial fits for the spherical and deformation valence density of chemically distinct atoms were optimized by refinement of their expansion–contraction parameters κ and κ', respectively The radial terms used for the Cu atoms were either simple Slater functions or the relevant order Fourier–Bessel transforms of the Su and Coppens[32] wave functions. It is well established[33] that the 3d transition metals present special problems when modeling the deformation density because of the significantly different radial extensions of the 3d and 4s valence orbitals. As a result, the 4s scattering is only significant for $(\sin\theta)/\lambda < 0.2$, and the reflections in this range often suffer more seriously from systematic errors such as extinction and absorption. It is therefore normally difficult to obtain a reliable estimate of the 4s population from diffraction data. The default treatment of the transition metals in the XD program assumes the 4s population to be part of the core density population $\rho_c(\mathbf{r})$, which is not refined. Attempts were made to refine a 4s population by using the second monopole, with a Slater radial function appropriate for 4s density. These refinements normally gave a negative monople population (suggesting that some 4s density should be removed from the core), but the overall fits and difference Fourier maps were not convincingly better. A number of models for the Cu atom were examined (by refinement against both experimental and synthetic static structure factors), including the use of a Cu^{2+} scattering model, but in the final analysis, it was decided to utilize the default [Ar]$4s^1$ neutral atom configuration to construct the core scattering factor for Cu, and the $3d^n$ configuration for the deformation radial functions. This somewhat arbitrary treatment of the Cu atom scattering translates into an ambiguity in the derived charge of the metal.

Isotropic secondary extinction corrections according to the Becker–Coppens formalism[35] (type I, Lorentzian distribution of mosaic spread) were applied to the data sets for all complexes. For complex **1**, the two most intense reflections (2 0 0) and (0 0 2) suffered from serious extinction effects in both data sets, which could not be adequately corrected for. As a consequence, these two reflections were removed from the refinement, because their inclusion could bias the least-squares procedure and hence the derived parameters.

The rigid-bond criterion of Hirshfeld[36] was applied to all covalent bonds involving non-H atoms and used to gauge the efficacy of the multipole refinements. For the light-atom−light-atom bonds, all the Δ-msda's were below 1.0×10^{-3} Å^2. The largest individual values for the standard covalent bonds involving Cu were for Cu1−O2, with Δ-msda values of 2.5, 1.8, and 1.7×10^{-3} Å^2 in **1**, **2**, and **3**, respectively. As expected, the weaker Cul···O3 interactions gave much larger Δ-msda's, in the range $3-9 \times 10^{-3}$ Å^2. Investigative refinements performed by using anharmonic thermal parameters on the Cu centers gave no improvement, and any anharmonicity in the thermal motion was henceforth ignored.

The kinetic energy densities at the bcp's $G(\mathbf{r})$ given in Table 3 for the experimental densities were estimated by using the approximation of Abramov[37]

$$G(\mathbf{r}) = (3/10)(3\pi^2)^{2/3}\rho(\mathbf{r})^{5/3} + (1/6)\nabla^2\rho(\mathbf{r}) \qquad (3)$$

whereas the corresponding potential energy densities at the bcp's $V(\mathbf{r})$ were obtained from the local virial theorem

$$V(\mathbf{r}) = (1/4)\nabla^2\rho(\mathbf{r}) - 2G(\mathbf{r}) \qquad (4)$$

The Abramov approximation for $G(\mathbf{r})$ holds well in regions where $\nabla^2\rho(\mathbf{r}) > 0$[38] and is a good approximation for the Cu−O and Cu−N bonds in **1**−**3** (see below). It is much less reliable for bonds involving shared interactions, such as C−C and C−H bonds.

A very important criterion for assessing the quality of the experimental data and the efficacy of the least-squares fit is the difference Fourier map, which should be flat and featureless.[39] The extrema in these maps are given in Table 1, peak listings are presented in Tables S1−S4 in the Supporting Information, and map sections through the Cu(1)−O(1)−N(1) and Cu(1)−O(2)−O(3) planes are presented in the Figures S4−S7 in the Supporting Information. The maps are somewhat noisier than might be expected for data involving first-row transition metals, and this is particularly so for complex **1** (this was one of the reasons for obtaining a second data set). However, a few comments are in order. The magnitudes of Δρ in difference Fourier maps are very sensitive to two criteria: (i) the resolution in reciprocal space of the data used for the summations and (ii) the digital resolution (i.e., the grid spacing in Å) of the computed map. The first values for Δρ given in Table 1 result from maps computed with all data having $F > 4\sigma(F)$ and with a grid spacing of 0.1 Å along all three crystallographic axes: these criteria effectively maximize |Δρ|. It is relatively uncommon for authors to state either of these criteria when quoting residual densities, though a $(\sin\theta)\lambda$ cutoff of 0.8 Å^{-1} in experimental charge density studies is commonly used.[9a,16b,40] Reducing the resolution of the map results in cosmetically smaller residuals, as seen in the second set of values listed in Table 1, which used a grid spacing of 0.2 Å and with $(\sin\theta)/\lambda \leq 0.8$ Å^{-1}. The highest +ve feature appears at the same place in the maps obtained from the APEX II and KappaCCD data for **1**, which were measured on different crystal specimens. This is indicative of a persistent problem in the crystal quality, most likely a very minor disorder. Figure S5 (Supporting Information) shows a representative distribution plot of residual density pixel values in the Fourier maps for complex **1**. In the absence of any systematic errors or under-modeling, the plot should be centered around 0 e Å^{-3} with a normal (Gaussian) distribution due to experimental noise.[39] There is a small tail above the idealized Gaussian distribution, in both the positive and the negative directions. It should be stressed that the highest |Δρ| features in all the maps are very sharp and represent only a tiny electron population. For example, for the noisiest data set (compound **1,** APEX II data), the total integrated electron populations for all pixels >0.5 and <−0.5 e Å^{-3} are only 0.13 and 0.18 e, respectively, that is, 0.017 and 0.024%, respectively, of the total electron population in the unit cell.

Scatterplots of the individual scale factors after the final multipole refinements and their corresponding binned plots (see Supporting Information, Figures S1 and S2) show no serious systematic deviations from linearity, apart from small deviations at the highest resolution These plots compare very favorably with similar plots obtained from a number of charge density data sets recently analyzed by Pinkerton et al.[41] The most obvious feature in the difference Fourier maps for **1** (APEX-II) is the highly negative residual close to the Cu nucleus. The most likely reason for this is a nonlinearity in the scale factor. The scatterplot of F^2(APEX-II)/F^2(KappaCCD) for individual reflections against $(\sin\theta)/\lambda$ (Figure S3 in the Supporting Information) shows that, at the lowest resolution ($(\sin\theta)/\lambda < 0.45$), the scale factor for the APEX-II data is consistently larger than that for the KappaCCD data. This nonlinearity throughout the resolution range appears to be a problem with some data collected on CCD diffractometers.[30b,41,42] Any ambiguity in the scale factor can have a seriously deleterious effect on derived charge density parameters such as the dipole moment.[30b] Despite these evident problems with the APEX-II data for **1**, we do not observe any consistent discrepancies between the topological properties obtained for **1** (see below).

Theoretical Studies. Single-point unrestricted DFT wave functions were obtained by using the GAUSSIAN03 program[43] at the experimental geometries of complexes **1**−**3**, in a pseudo gas-phase calculation. To model the full environment of the Cu(II) ions, the pendant anions were also included in the calculations, and to avoid problems with an overall negative charge, the Cu(II) ions from adjacent complexes (which are attached to the pendant L$^-$ anions) were replaced by protons, so as to yield an electroneutral complex, that is,[$Cu_2(ap)_2(L)_2(HL)_2$]. Calculations for the broken symmetry singlet and triplet states were undertaken within the B3LYP hybrid functional, deploying 6-311++G(2d,2p) basis sets for H, C, N, and O atoms and a Wachters+f basis for the Cu atom.[44] In all three cases, the broken symmetry singlet state emerged as the ground state, with triplet−singlet energy separations ($E_t - E_s \approx -2J$) of 337, 474, and 313 cm^{-1}, respectively, for **1**−**3**. Although these values constitute overestimates of the experimental splittings, their relative ordering is correct. More realistic estimates of the coupling strengths are obtained from the periodic calculations discussed below. The topology and integrated properties of the Kohn−Sham densities were analyzed by using the AIMPAC[45] and AIM2000[46] programs. There were only very minor differences in the topological properties of the densities obtained from the (nonphysical) broken symmetry singlet and the triplet wave functions. The experimental magnetic coupling values ($-2J$) reported[12a,13] for complexes **1**−**3** imply only a fractional population ($<10^{-3}$) of the triplet state at 100 K. Because the primary purpose of these calculations was to provide a reference for comparison with the experimentally derived densities, we quote here the results from the ground-state antiferromagnetic singlet computations. Complex static X-ray structure factors to a resolution of $(\sin\theta)/\lambda \leq 1.1$ Å^{-1} were obtained from the molecular wave function by numerical integration of the charge density for reciprocal lattice points corresponding to a pseudocubic unit cell with $a = 30$ Å obtained by using the program

WFN2HKL.[47] Multipole refinements performed by using XDLSM against this data were undertaken to validate the transition metal model used for the experimental data.

To obtain further insight into the magnetism of these lattices, periodic B3LYP functional calculations were undertaken within the CRYSTAL06[48] code for complexes **2** and **3**, the unit cells of which are of tractable size. The experimentally determined atomic coordinates were used without optimization. The crystalline orbitals were expanded in terms of standard 6-31G basis sets, whereas the band structure was sampled upon a Monkhorst−Pack mesh[49] with an 8-fold shrinking factor. A total energy convergence tolerance of 10^{-9} E_h provided coupling constants of adequate precision. As in the molecular calculations, static X-ray structure factors to a resolution of $(\sin \theta)/\lambda \leq 1.1$ Å^{-1} were computed from the periodic wave function, and multipole refinements were subsequently performed by using the XDLSM code.

Results and Discussion

Description of the Structures. ORTEP diagrams for complexes **1**−**3** are shown in Figure 1. As previously discussed,[12] the Cu(II) ions are strongly Jahn−Teller distorted. The primary coordination sphere of the Cu atoms (Table 2) is a square-planar arrangement of four strongly bonded ligators atoms in the *xy* plane (N and O atoms from the 3-aminopropanolate and an O atom from the L$^-$ anion), in which the Cu−X distances all lie below 2.05 Å. In the solid state, one axial coordination site is occupied by another O atom of a pendant L$^-$ anion from an adjacent complex in the lattice, at a significantly longer distance of 2.5−2.6 Å. The second axial coordination site could potentially be considered as occupied by an additional O atom from the L$^-$ anion. However, the angle subtended at the Cu(II) center is much smaller than 90°, and the corresponding Cu1···O3 distances are quite variable in the three complexes, being the shortest in the nitrite complex **1** and the longest in the formate complex **3**. There is an inverse correlation between the Cu1···O3 and Cu1···O3^{ii} distances for these two weakly coordinating interactions, (see Table 2). As discussed below, the charge density evidence for any significant Cu···O3 interaction is ambiguous at best.

Because of the crystallographic inversion center, the four atoms of the central $Cu_2(\mu\text{-}O)_2$ unit are necessarily coplanar in all three complexes. The planarity of the primary coordination sphere of the Cu atoms is then quantified by the torsion angles Cu1−O1−Cu1^i−O2^i and Cu1−O1^i−Cu1^i−N1^i, which are given in Table 2. We note that these should amount to 180° for a perfectly coplanar arrangement. The nitrate complex **2** is closest to planarity, whereas the formate complex **3** shows the greatest deviation, with the O2 atom lying significantly out of the plane defined by the remaining three ligator atoms. The θ and τ angles, as defined by Ruiz et al.[5c] for the central $Cu_2(\mu\text{-}O)_2$ unit, are also given in Table 2 and are very similar for all three complexes.

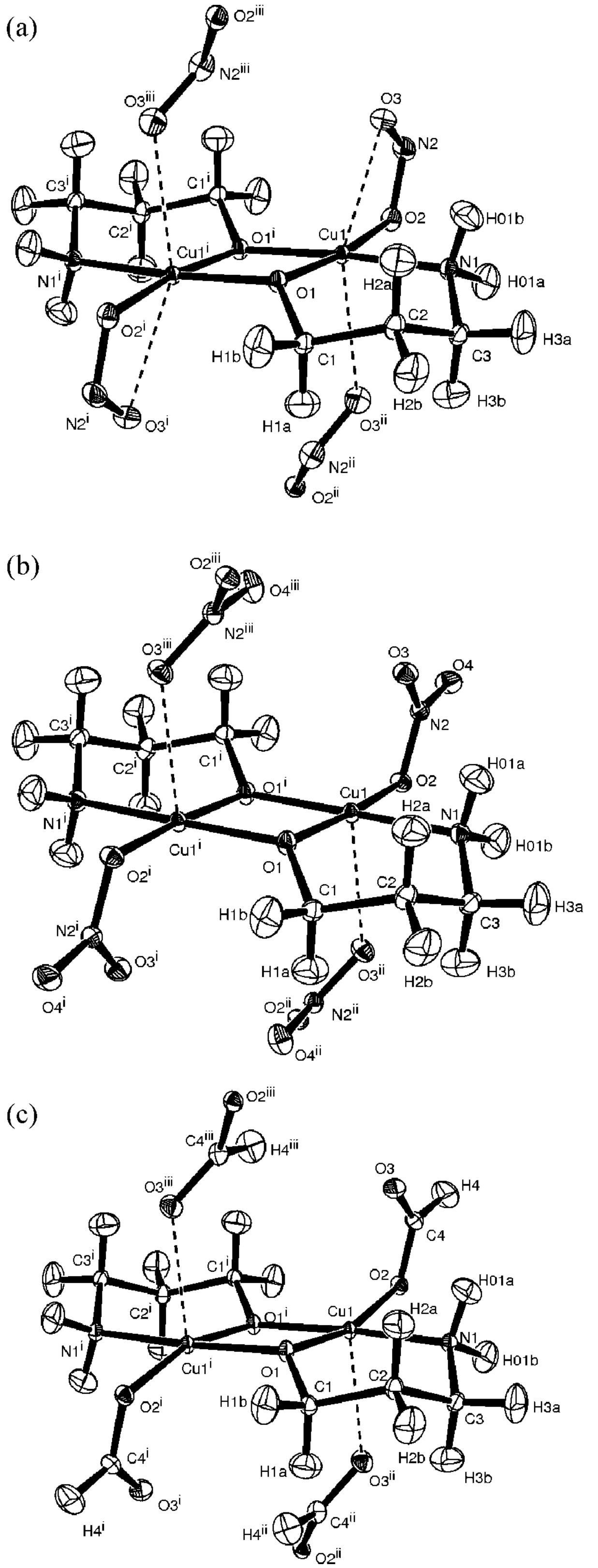

Figure 1. ORTEP plot of **1** showing the atomic labeling scheme, with thermal ellipsoids drawn at the 50% probability level. Symmetry codes: (a) (i) $2 - x, 1 - y, -z$; (ii) $-1/2 + x, 3/2 - y, -z$; (iii) $5/2 - x, -1/2 + y, z$; (b) (i) $-x, -y, 1 - z$; (ii) $-x, 1/2 + y, 3/2 - z$; (iii) $x, -1/2 - y, -1/2 + z$; (c) (i) $-x, 1 - y, -z$; (ii) $-x, 1/2 + y, 1/2 - z$; (iii) $x, 1/2 - y, -1/2 + z$.

The unit-cell packing motifs in complexes **1**−**3**, Figure S12 in the Supporting Information, are closely similar, and complexes **2** and **3** present a particularly interesting case. They share the same space group $P2_1/c$, and the fractional coordinates of corresponding atoms are very similar, but because their unit cells are significantly different (because of H-bonding, see below), they are not truly isomorphous. A partial packing diagram for **3** is shown in Figure 2. Each dimer unit **A** is surrounded by four others (**B**, **B′**, only two are shown in Figure 2) which complete the coordination sphere of the Cu(II) ions through the pendant L$^-$ anions. A further two dimers **C**, related by unit cell translations along the *b* axis for **1** and *c* axis for **2** and **3**, are connected to the central **A** dimer by H-bonding ring networks. These ring linkages are described in the Etter

TABLE 2: Coordination Geometry (Angstroms, Degrees)

	1[a]	**2**	**3**
Cu1$\cdots$Cu1^{i}	2.96329(17)	2.95640(11)	2.97844(12)
Cu1−N1	1.9813(4)	1.9710(3)	1.9871(3)
Cu1−O1	1.9389(4)	1.9265(3)	1.9474(2)
Cu1−O1^{i}	1.9368(4)	1.9270(3)	1.9375(3)
Cu1−O2	2.0197(6)	2.0132(3)	1.9933(3)
Cu1$\cdots$O3	2.4762(6)	2.5943(4)	2.6920(5)
Cu1$\cdots$O3^{ii}	2.6042(7)	2.5692(4)	2.4790(5)
Cu1−O1−Cu1^{i} (θ angle)	99.738(19)	100.207(14)	100.111(11)
O1−Cu1−O1^{i}	80.262(19)	79.793(14)	79.889(11)
O1−Cu1−N1	95.906(19)	95.782(13)	95.652(11)
O2−Cu1−N1	90.94(2)	90.668(14)	89.559(12)
O2−Cu1−O1^{i}	93.16(2)	93.760(14)	95.366(12)
O1−Cu1−O3^{ii}	91.68(2)	97.152(15)	93.338(14)
O1^{i}−Cu1-O3^{ii}	92.81(2)	95.833(15)	92.726(14)
O2−Cu1−O3^{ii}	93.33(2)	83.170(14)	100.999(14)
N1−Cu1−O3^{ii}	83.71(2)	85.846(13)	85.039(13)
O1^{i}−O1-C1 (τ angle)	31.88(5)	28.62(4)	29.22(3)
Cu1−O1−Cu1^{i}-O2^{i}	175.3(1)	179.8(1)	165.8(1)
Cu1−O1^{i}-Cu1^{i}-N1^{i}	176.4(1)	178.8(1)	177.5(1)

[a] Taken from APEX II refinement.

notation[50] as $R_2^2(8)$ for **1** and **3** and $R_2^2(12)$ for **2**. This arrangement results in polymerized layers lying parallel to the *ab*-plane in **1** and to the *bc*-plane in **2** and **3** and involves only two crystallographically independent dimer−dimer interactions, **A**$\cdots$**B** and **A**$\cdots$**C** (see Figure 2). The larger ring network for complex **2** results in a longer *c*-axis compared with that for **3** and differentiates their crystal packing which is otherwise extremely similar.

Topological Description of the Chemical Bonding. The QTAIM developed by Bader and co-workers[6] characterizes the charge density $\rho(\mathbf{r})$ in terms of local properties at the critical points in the scalar field, where $\nabla\rho(\mathbf{r}) = 0$. The Laplacian of the charge density $\nabla^2\rho(\mathbf{r})$ also adopts an important position in QTAIM, in view of expression 4 given above. It measures the local relationship between the kinetic energy density $G(\mathbf{r})$ (everywhere positive) and the potential energy density $V(\mathbf{r})$ (everywhere negative). If $V(\mathbf{r})$ dominates, $\nabla^2\rho(\mathbf{r})$ is negative, which is indicative of a shared-shell (covalent) interaction, whereas if the opposite situation pertains, a closed-shell interaction results.[51] This bipolar classification of chemical bonding is very useful for compounds of the second periodic row but is less useful for compounds containing heavier elements, in particular the transition metals. For these elements, the bond critical point invariably falls in a region of charge depletion, but this should not be naively taken as indicative of a closed-shell (ionic) interaction.[52] For these situations, a number of other topological criteria need to be examined in order to fully characterize the chemical bond. These criteria include the topology of $\nabla^2\rho(\mathbf{r})$ along the bond path, the delocalization index δ(A,B),[53] the local energy densities $H(\mathbf{r}_b)$,[54] and the integral $N(\mathrm{A,B}) = \oint_{A\cap B} \rho(\mathrm{r})$ of the density over the zero flux surface shared by the two atoms.[54]

A topological analysis of the experimental charge density in the complexes **1**−**3** was undertaken by using the molecule-extracted-from-crystal approach in the XDPROP program.[29] The dimeric complex, together with the two pendant L anions, were included in the analysis so as to account for the full coordination sphere of the Cu atoms. All the expected bond critical points (bcp's) corresponding to the strong covalent bonds in the dimeric complex were observed. Those involving the Cu(II) centers are listed in Tables 3 and 4, and a full listing of all critical points is given in Tables S8−S14 in the Supporting Information. The experimental and theoretical molecular graphs for complexes **1** and **3** are illustrated in Figures 3 and 4, respectively, and those for **2** are given in the Supporting Information.

The agreement between theory and experiment for the magnitudes of $\rho(\mathbf{r_b})$ and $\nabla^2\rho(\mathbf{r}_b)$ is in general excellent, as is evident from the strong similarity in the experimental and theoretical Laplacian plots (shown in Figure 5 for complex **1**). Eickerling et al.[55] have recently observed that for transition-metal complexes "the general agreement between experimental and theoretical values of $\rho(\mathbf{r_b})$ and $\nabla^2\rho(\mathbf{r_b})$ typically lie in the range 0.01−0.03 and 0.77−1.13 eÅ^{-5}, respectively". From the values given in Tables 2 and 3, the mean discrepancies for $\rho(\mathbf{r_b})$ and $\nabla^2\rho(\mathbf{r}_b)$ are 0.03 and 0.43 eÅ^{-5}, respectively, which agrees well with this observation. For the Cu−O interactions, the experimental values of $\rho(\mathbf{r}_b)$ are systematically slightly lower than the comparable theoretical results, though this is not the case for the Cu−N interactions. The experimental and theoretical values of $\rho(\mathbf{r_b})$ for the Cu−N bonds are marginally greater than for the Cu−O1 bonds despite being slightly longer, suggestive of an increased covalent character. Moreover, the polarization of the N atoms towards the Cu centers is significantly greater, as may be seen in Figure 5.

The ellipticity ε of the charge density at the bcp[56] is useful in indicating π-bond character in main-group−main-group bonds,[6] but its interpretation is more problematic for transition-metal ligator bonds. The experimental values show a much greater spread than the theoretical values because of the difficulties involved in obtaining accurate experimental estimates of the second-order derivative $\nabla^2\rho(\mathbf{r}_b)$. The mostly low ε values obtained from the theoretical topologies suggest little evidence for Cu-ligand π-bonding. Notably, the largest ε in both experiment and theory is characteristically associated with the Cu$\cdots$O(3) interaction in complex **1**, which is a topologically unstable feature as discussed below.

The experimental values for the total energy densities $E(\mathbf{r}_b)$ are around 0 for the Cu−O bonds but consistently more negative for the Cu−N bonds. This is consistent with a greater covalent character for the latter bonds, as we have observed previously[57] for the Ni−O and Ni−N bonds in the Ni(II) coordination complex $[\mathrm{Ni(H_3L)}][\mathrm{NO_3}][\mathrm{PF_6}]$ {$\mathrm{H_3L}$ = *N*,*N′*,*N″*-tris(2-hydroxy-3-methyl butyl)-1,4,7-triaza-cyclononane}. In the theoretical study, the values for $E(\mathbf{r}_b)$ are all negative, consistent with some covalent character for all bonds, but again, the Cu−N bonds have the most negative values. The experimental values of $|V(\mathbf{r}_b)|/G(\mathbf{r}_b)$ are ∼1.0 for the strong Cu−O bonds and slightly less for the weak Cu−O interactions, whereas the corresponding theoretical values are all marginally greater than 1. For the Cu−N bonds, $|V(\mathbf{r}_b)|/G(\mathbf{r}_b)$ is ∼1.1 in both the experimental and theoretical studies. Within the classification proposed by Espinosa et al.,[58] this indicates a transitional interaction, between pure closed-shell and shared-shell.

The molecular graphs shown in Figures 3 and 4 illustrate several points of interest. First, and most importantly, there is no evidence for any direct Cu−Cu interaction, as indicated by the lack of a bcp between these two centers. Instead, a (3, +1) cp in $\rho(\mathbf{r})$ is found at the Cu−Cu midpoint, denoting a ring structure for the $\mathrm{Cu_2}(\mu\text{-O})_2$ moiety. This ring structure is clearly illustrated by the gradient vector plot shown in Figure 6 and is consistent with the notion that the magnetic coupling between the two centers is mediated almost entirely by the bridging O atoms. An exactly analogous situation regarding the Cu$\cdots$Cu interaction was observed by Lecomte and co-workers[9a] in $\mathrm{Cu_2(OH)_3NO_3}$. The lack of any direct Cu$\cdots$Cu bonding interaction is corroborated by the source function, discussed below, and also by the insignificant value of the delocalization index[53] δ(Cu−Cu′) = 0.02 obtained in complex

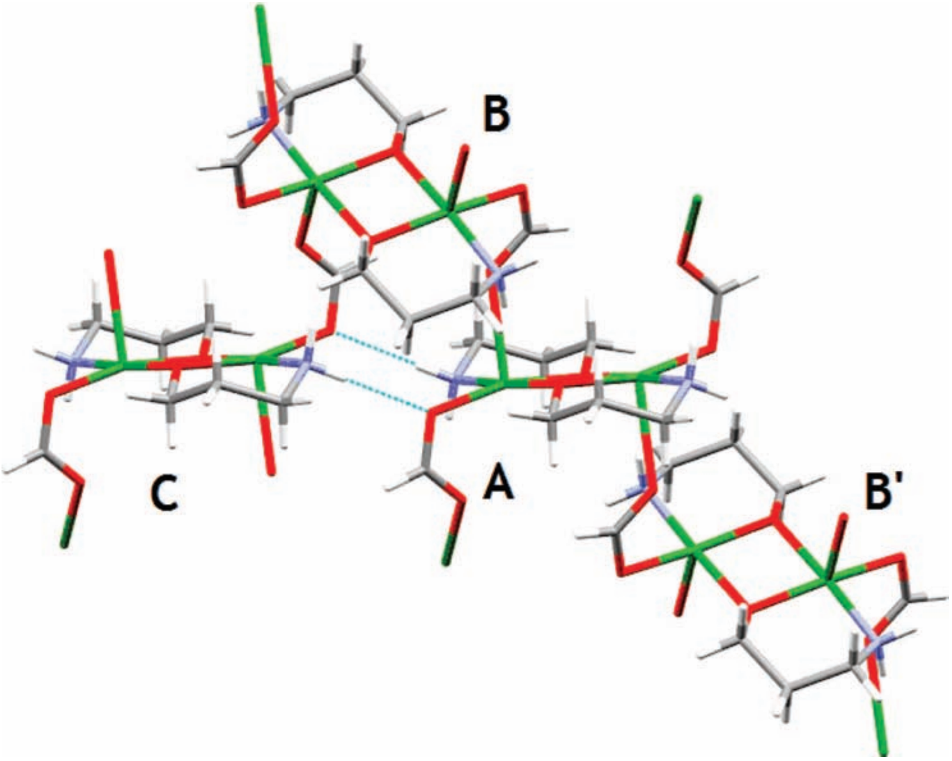

Figure 2. Partial packing diagram of complex **3**, showing the N−H···O hydrogen bonding network (blue dashed lines, dimer−dimer interaction A···C) and the completion of the coordination sphere around Cu ions, dimer−dimer interaction A···B. Color scheme: Cu, green; O, red; N, blue; C, gray; H, white.

TABLE 3: Experimental Topological Parameters for Bond Critical Points Involving Copper[a]

d1[b]	d2[b]	$\rho(\mathbf{r}_b)$[c]	$\nabla^2\rho(\mathbf{r}_b)$[d]	λ_1[d]	λ_2[d]	λ_3[d]	ε	$G(\mathbf{r}_b)$[e f]	$G(\mathbf{r}_b)/\rho(\mathbf{r}_b)$	$V(\mathbf{r}_b)$[e]	$\lvert V(\mathbf{r}_b)\rvert / G(\mathbf{r}_b)$	$E(\mathbf{r}_b)$[e]
	Cu1−O1											
0.9435	0.9959	0.57	12.78	−2.82	−1.93	17.54	0.46	0.91	1.60	−0.93	1.02	−0.02
0.9495	0.9907	0.53	12.53	−2.55	−1.92	17.01	0.33	0.86	1.64	−0.84	0.98	0.02
0.9643	0.9625	0.58	12.60	−2.79	−2.50	17.89	0.11	0.91	1.58	−0.94	1.03	−0.03
0.9614	0.9869	0.54	11.72	−2.71	−2.23	16.66	0.22	0.84	1.54	−0.85	1.01	−0.02
	Cu1−O1^{i}											
0.9462	0.9923	0.59	13.03	−2.71	−2.07	17.81	0.31	0.94	1.60	−0.96	1.02	−0.03
0.9535	0.9865	0.53	12.38	−2.59	−2.12	17.08	0.22	0.86	1.61	−0.85	0.99	0.01
0.9524	0.9751	0.58	13.23	−2.92	−2.56	18.70	0.14	0.94	1.62	−0.96	1.02	−0.02
0.9579	0.9804	0.62	12.46	−3.29	−2.83	18.58	0.17	0.94	1.53	−1.01	1.05	−0.07
	Cu1−O2											
0.9824	1.0373	0.46	10.07	−2.08	−1.39	13.53	0.50	0.69	1.50	−0.67	0.97	0.02
0.9876	1.0342	0.45	9.91	−2.15	−1.59	13.65	0.33	0.68	1.50	−0.66	0.97	0.02
0.9990	1.0142	0.48	10.15	−2.33	−1.99	14.47	0.17	0.71	1.48	−0.71	1.00	0.00
0.9775	1.0164	0.50	10.36	−2.41	−2.16	14.93	0.12	0.73	1.48	−0.74	1.00	−0.01
	Cu1−O3[g]											
1.2406	1.2394	0.20	2.92	−0.58	−0.14	3.64	3.25	0.19	0.96	−0.18	0.95	0.01
	Cu1−O3^{ii}											
1.3028	1.3028	0.15	1.88	−0.54	−0.43	2.84	0.25	0.12	0.80	−0.11	0.92	0.01
1.3083	1.3007	0.13	1.72	−0.39	−0.36	2.46	0.08	0.11	0.83	−0.09	0.82	0.01
1.2948	1.2749	0.14	1.95	−0.43	−0.42	2.80	0.02	0.12	0.87	−0.11	0.92	0.02
1.2433	1.2364	0.17	2.46	−0.56	−0.54	3.56	0.03	0.15	0.94	−0.14	0.93	0.02
	Cu1−N1											
0.9353	1.0495	0.68	10.86	−2.79	−2.35	16.00	0.19	0.93	1.37	−1.10	1.18	−0.17
0.9449	1.0388	0.60	10.93	−2.57	−2.15	15.65	0.20	0.85	1.42	−0.95	1.12	−0.09
0.9480	1.0233	0.64	10.64	−2.93	−2.72	16.29	0.07	0.88	1.37	−1.01	1.15	−0.13
0.9664	1.0208	0.62	10.13	−3.05	−2.93	16.11	0.04	0.84	1.35	−0.99	1.15	−0.13

[a] Lines 1−4, experimental values for **1**(APEX II), **1**(KappaCCD), **2**, **3**, respectively. [b] In units of Å. [c] In units of e Å^{-3}. [d] In units of e Å^{-5}. [e] In units of Hartree Å^{-3}. [f] Estimated by the approximation of Abramov.[37] [g] bcp only observed for **1** (APEX II).

2. This may be compared with the values δ(Cu−O1) = 0.51/0.47 and δ(Cu−N1) = 0.51 for the strong covalent bonds involving the Cu atom, which are quite typical[52a] of transition-metal−ligator interactions. Moreover, the value of δ(Cu−Cu′) remains insignificant even in comparison with the weak Cu···O3 and Cu···O3^{ii} interactions, for which δ(Cu−O3) = 0.10 in both cases. Following the interpretation of Pendás et al.[11] mentioned above, the bond paths linking the Cu atoms

TABLE 4: Theoretical Topological Parameters for Bond Critical Points Involving Copper[a]

d1[b]	d2[b]	$\rho(\mathbf{r}_b)$[c]	$\nabla^2\rho(\mathbf{r}_b)$[d]	λ_1[d]	λ_2[d]	λ_3[d]	ε	$G(\mathbf{r}_b)$[e]	$G(\mathbf{r}_b)/\rho(\mathbf{r}_b)$	$V(\mathbf{r}_b)$[e]	$\lvert V(\mathbf{r}_b)\rvert/G(\mathbf{r}_b)$	$E(\mathbf{r}_b)$[e]
	Cu1−O1											
0.9403	0.9992	0.60	12.42	−2.88	−2.79	18.09	0.04	0.91	1.53	−0.96	1.05	−0.04
0.9342	0.9928	0.62	12.73	−3.02	−2.92	18.66	0.03	0.94	1.53	−1.00	1.06	−0.05
0.9433	1.0045	0.58	12.11	−2.78	−2.68	17.58	0.04	0.89	1.52	−0.92	1.04	−0.04
	Cu1−O1′											
0.9379	0.9993	0.59	12.44	−2.84	−2.75	18.03	0.04	0.91	1.54	−0.95	1.04	−0.04
0.9345	0.9930	0.60	12.83	−2.94	−2.84	18.60	0.04	0.94	1.56	−0.99	1.05	−0.04
0.9380	1.0000	0.59	12.46	−2.80	−2.73	17.99	0.03	0.91	1.55	−0.95	1.04	−0.04
	Cu1−O2											
0.9712	1.0490	0.51	9.50	−2.40	−2.20	14.10	0.09	0.69	1.36	−0.72	1.04	−0.03
0.9649	1.0486	0.50	10.06	−2.35	−2.13	14.54	0.11	0.73	1.44	−0.74	1.01	−0.02
0.9588	1.0350	0.53	10.47	−2.48	−2.32	15.27	0.07	0.76	1.43	−0.79	1.04	−0.03
	Cu1−O3[f]											
1.2248	1.2524	0.21	2.24	−0.67	−0.39	3.29	0.73	0.19	0.90	−0.22	1.16	−0.03
	Cu1−O3′											
1.2715	1.3342	0.14	1.48	−0.44	−0.42	2.33	0.06	0.12	0.86	−0.13	1.10	−0.01
1.2586	1.3125	0.14	1.59	−0.47	−0.45	2.51	0.06	0.13	0.88	−0.14	1.08	−0.01
1.2331	1.2472	0.17	2.02	−0.58	−0.57	3.16	0.02	0.16	0.92	−0.18	1.12	−0.02
	Cu1−N1											
0.9443	1.0373	0.61	10.40	−2.75	−2.66	15.82	0.04	0.82	1.35	−0.92	1.12	−0.10
0.9408	1.0299	0.63	10.61	−2.88	−2.80	16.29	0.03	0.85	1.35	−0.96	1.13	−0.11
0.9459	1.0413	0.60	10.27	−2.70	−2.60	15.57	0.04	0.81	1.35	−0.90	1.11	−0.09

[a] From gas-phase DFT wave function; lines 1−3, values for **1**, **2**, and **3**, respectively. [b] In units of Å. [c] In units of e Å^{-3}. [d] In units of e Å^{-5}. [e] In units of Hartree Å^{-3}. [f] bcp only observed for **1**.

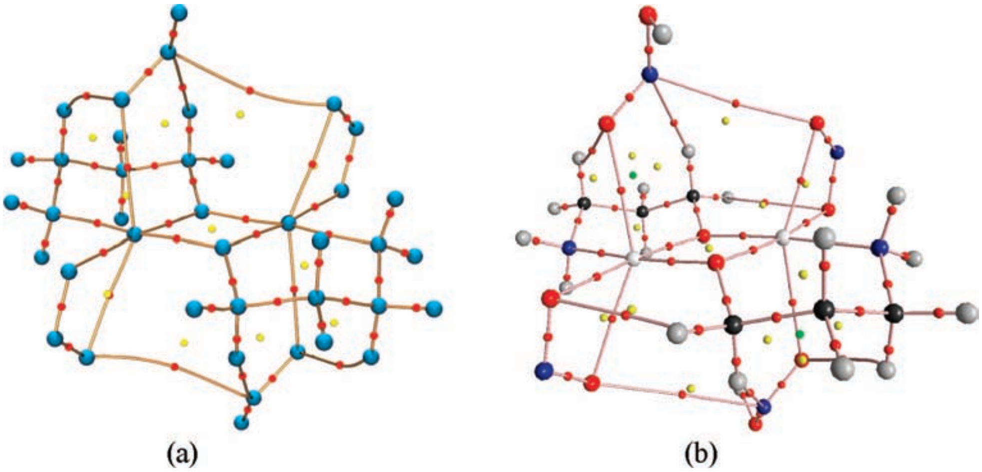

Figure 3. Experimental (a) and theoretical (b) molecular graphs for complex **1**, in the same view as that in Figure 1. Critical points in $\rho(\mathbf{r})$ are shown as small red spheres for (3, −1), yellow spheres for (3,+1), and green spheres for (3,+3). The atomic positions are shown as blue spheres in (a) and are colored by individual element in (b).

via the bridging O atoms can be seen to provide strong experimental evidence for the superexchange pathway.

The experimental and theoretical molecular graphs are virtually identical, even to the extent of the weak interactions linking the pendant anions and dimer units. In fact, the only qualitative discrepancies are the lack of any (3,+3) cage critical points, and the absence of one long-range CH···O interaction, in the experimental topology. The pendant L$^-$ anion displays four bond paths to the dimer unit in all three complexes, viz (i) an almost linear path between the weakly coordinating O atom and the Cu center, (ii) a curved bond path between this same O atom and the closest H atom of the CH$_2$ group bonded to the amine, (iii) a CH···X interaction involving the CH$_2$ group bonded to the bridging O atom, where X is the N atom of the nitrito or nitrato ligand in complexes **1** and **2**, or the H atom of the formate anion in **3**, and (iv) an unusual N···O or H···O interaction between the pendant and strongly coordinated L$^-$ anions. These four bond paths represent the main interaction pathways in the dimer−dimer interaction of type A−B (and A−B′) shown in Figure 2, the only additional bond path being due to a weak N−H···O2 H-bond.

The molecular graphs also show several instances of unstable topological features, close to a fold catastrophe point.[6] These catastrophe points generally arise in regions of low, flat density where a (3,−1) bcp and the associated (3,+1) rcp have very similar densities and are physically close together in space. A slight perturbation in configuration space can lead to the coalescence of the bcp and rcp and hence to the elimination of the bond path. Such unstable topological features are typically associated with high bond ellipticities ε, and complex **1** is a case in point. The Cu(1)···O(3) bond path, which is observed in the theoretical molecular graph of **1** and the experimental one derived from the refinement performed by using the APEX II data (Figure 3) is missing from the graph obtained from the refinement performed by using the KappaCCD data. The densities at the bcp (0.198 eÅ^{-3}) and the associated ring cp (0.197 eÅ^{-3}) are virtually identical, and the cp's are separated by only 0.081Å. It is not clear why the refinements against the

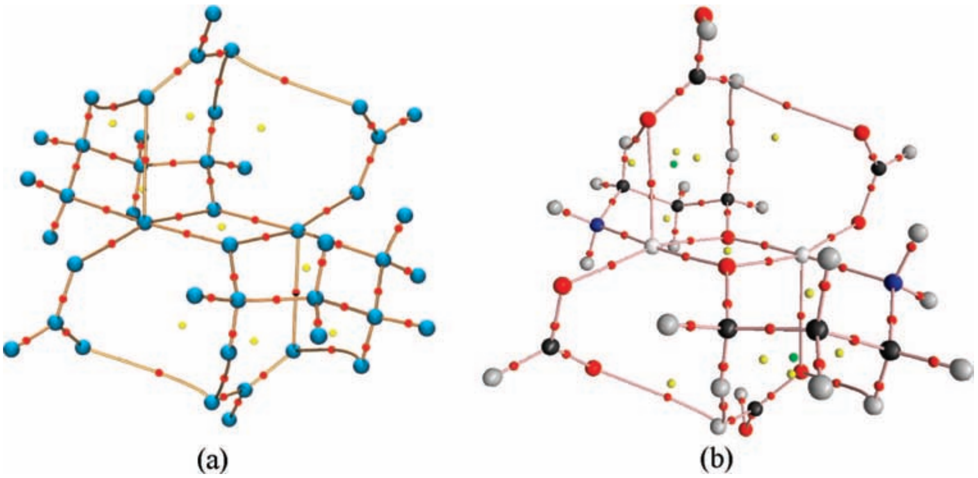

Figure 4. Experimental (a) and theoretical (b) molecular graphs for complex **3**, in the same view as that in Figure 1. Critical points in $\rho(\mathbf{r})$ are shown as small red spheres for (3, −1), yellow spheres for (3,+1), and green spheres for (3,+3). The atomic positions are shown as blue spheres in (a) and are colored by individual element in (b).

two experimental data sets give differing results. One possibility, which can be definitively excluded, is the differing resolutions of the two data sets. Refinement against both data sets truncated to $(\sin \theta)/\lambda \leq 1.0$ gave the same results as those obtained for the full data sets. The other unstable topological feature is the bond path associated with a CH···O interaction, corresponding to H(1B)···O(2)^{i} in Figures 1−3. This bond path is only observed in the theoretical graphs of **1** and **2** and in none of the experimental graphs. Again, the bcp and associated rcp are physically very close in space (0.084 Å for complex **1** and 0.064 Å for complex **2**). It is reasonable to suppose that these unstable topological features do not make a significant contribution toward the chemical bonding. We conclude that the topological evidence for any significant Cu···O3 interaction in these systems is marginal at best and that any such interaction would be primarily electrostatic in nature.

The unusual bond paths between the pendant L$^-$ anion and the dimeric unit described above are typical of weak inter (and intra)-molecular interactions, and such non-intuitive bond paths have been the focus of considerable debate in the literature.[10] In the complexes under consideration, we consider these bond paths to provide evidence for the mainly electrostatic nature of the interaction(s) between the pendant L$^-$ anion and the Cu dimer. Color-coded mapping of properties such as $\rho(\mathbf{r})$ or the electrostatic potential $\phi(\mathbf{r})$ onto molecular surfaces, such a van der Waals or density isosurfaces, provides a 3D appreciation of these properties with an immediate visual impact.[59] Spackman et al. have suggested that the Hirshfeld surface[60] provides a relatively unbiased molecular surface for displaying crystal interactions. This surface is nontessellated, but the Hirshfeld weight $w(\mathbf{r})$[61] used to define the surface is trivially computed as

$$w(\mathbf{r}) = \rho(\text{molecule})/\rho(\text{crystal}) = 0.5$$

where ρ is the sum of noninteracting atomic densities. We present in Figures 7 and 8 the experimental properties $\rho(\mathbf{r})$ and $\phi(\mathbf{r})$ mapped on the Hirshfeld surface for **2**. Analogous plots for complexes **1** and **3** are shown in Figures S15−S22 (Supporting Information). The molecular properties were calculated both for an isolated molecule and a molecule embedded in a cluster, to model the crystalline environment. The $\rho(\mathbf{r})$-mapped surfaces are very similar for the isolated molecule and the molecule-in-a-crystal calculations, but the $\phi(\mathbf{r})$-mapped

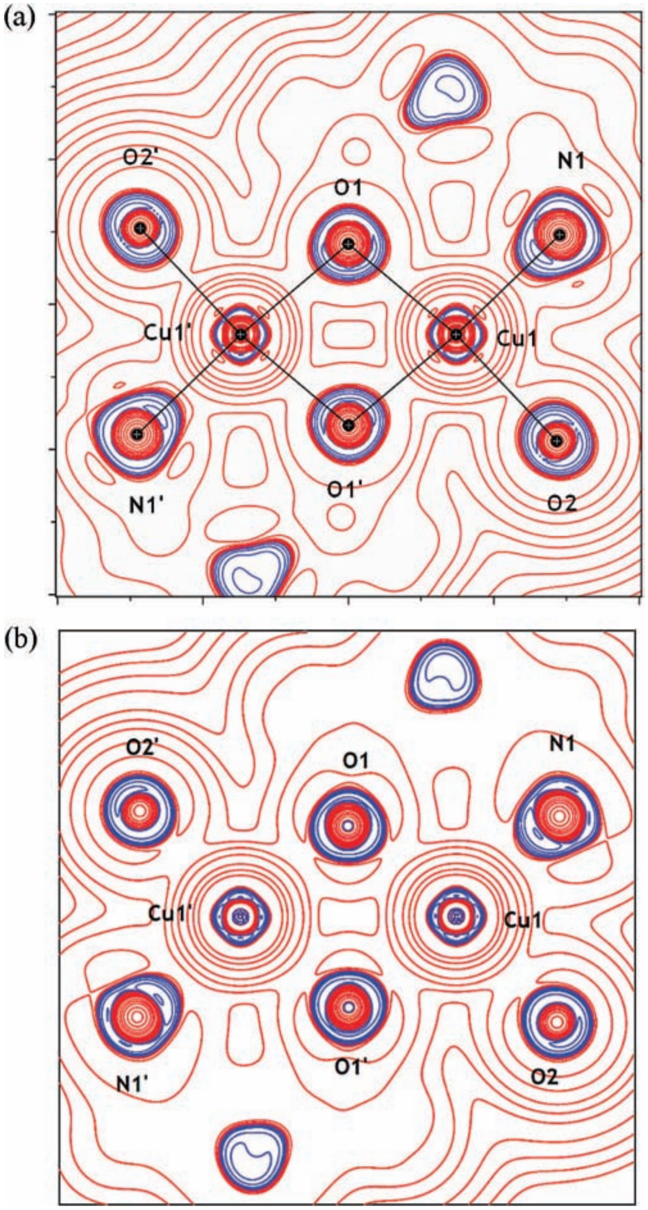

Figure 5. Plot of the (a) experimental and (b) theoretical Laplacian $\nabla^2\rho(\mathbf{r})$ in the $Cu_2(\mu\text{-}O)_2$ plane in complex **1**.

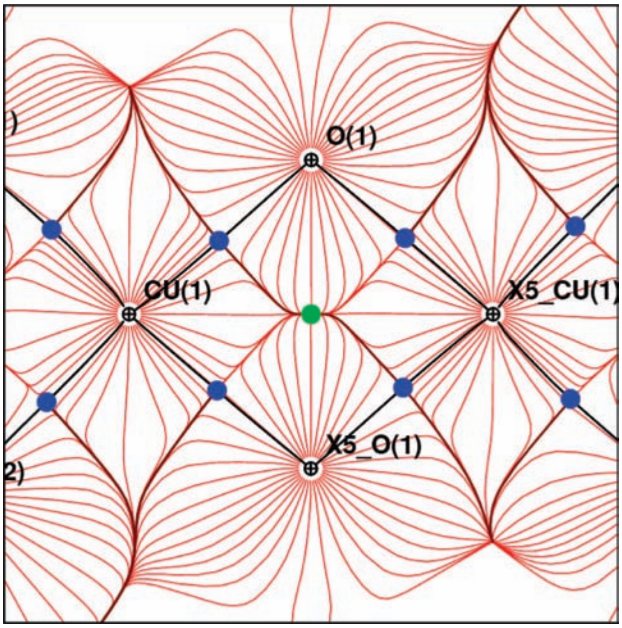

Figure 6. Plot of the experimental gradient vector field in the $Cu_2(\mu\text{-}O)_2$ plane in complex **1**. (3,−1) critical points in $\rho(\mathbf{r})$ are shown as blue spheres, and the (3,+1) critical point in $\rho(\mathbf{r})$ are shown as a green sphere.

surfaces are quite different as a result of the interaction of the molecular $\phi(\mathbf{r})$ with the electric potential of the crystal, which shifts $\phi(\mathbf{r})$ to more positive values. The intermolecular interactions are clearly visible in the $\rho(\mathbf{r})$-mapped surface, as points of relatively high density, but are not so obvious in the $\phi(\mathbf{r})$-mapped[60d] surface. Moreover, this latter surface provides an immediate visual appreciation of the great similarity in the crystal structures of **2** and **3** and also shows differences in $\phi(\mathbf{r})$ for the two experimental determinations for **1**, see Figures S15 and S17 (Supporting Information).

Finally, as pointed out by Macchi and Sironi,[52a] the integral $N(A,B) = \oint_{A\cap B} \rho(r)$ of the density over the zero-flux surface shared by the two atoms provides an index of the chemical bonding between atomic centers. Table 5 lists the values of this integral for the interatomic surfaces involving the Cu atom in **1**−**3**. As might be expected, the values are reasonably similar in all three complexes. For the strongly coordinated ligators, they are all greater than 1.0 $e\text{Å}^{-1}$, which indicates[52a] substantial electron sharing. Indeed, they are slightly larger than values of 1.02 and 0.87 $e\text{Å}^{-1}$ that we have previously reported[57] for the Ni−N/Ni-O bonds in a Ni(II) coordination complex. On the other hand, the surface integral for $Cu\cap O3^{ii}$, which involves the weakly coordinated pendant anion, is much smaller and is closely comparable with that reported[52a] for the ion pair Na^+F^-. This provides yet further compelling evidence for the essentially electrostatic nature of the weak $Cu-O3^{ii}$ interaction.

Source Function. Bader and Gatti[62] have shown that the electron density at any point **r** within a molecule may be viewed as arising from contributions from a source operating at all other points **r**′. The local source (LS) contribution at position vector **r** from **r**′ is given by

$$-(1/4\pi)\int \frac{\nabla^2\rho(\mathbf{r}')}{|\mathbf{r}-\mathbf{r}'|}\,d\mathbf{r}'$$

By integrating over the regions of space bounded by the zero-flux surfaces, the density may be equated to a sum of atomic contributions $S(\mathbf{r},\Omega)$.

$$\rho(\mathbf{r}) = \sum_{\Omega}\int_{\Omega} \mathrm{LS}(\mathbf{r},\mathbf{r}')\,d\mathbf{r}' \equiv \sum_{\Omega} S(\mathbf{r},\Omega)$$

The integrated form of the source function (SF) provides a measure of the relative importance of each atom's contribution to the density at a specific point. It has proved very useful in the characterization of different types of hydrogen bonds,[63] metal−metal interactions in bimetallic carbonyl complexes,[64] and metal−ligand interactions in $Fe(TMM)(CO)_3$.[26b] The reference points **r** are normally positioned at the bcp's, because these provide the least biased positions for inducing chemical bonding information from the SF. Figure 9 shows plots of the integrated SF obtained from the DFT calculation on **2**; the comparable plots for complexes **1** and **3** are essentially identical. Full tables of the percentage SF for all three complexes are given in the Supporting Information.

Broadly speaking, there are two general types of SF plot for complexes **1**−**3**. One is exemplified by Figure 9a, where the reference point is taken as the rcp between the Cu(II) centers. In this case, almost all of the atomic basins make a detectable contribution to $\rho(\mathbf{r})$, the largest individual contribution (in total ~26.5%) coming from the two Cu(II) centers. It is clear however that the SF is very delocalized, and even the atoms in the pendant anions (which are not connected by strong covalent bonds to the dimer unit) make some contributions. We interpret the charge density $\rho(\mathbf{r})$ at this reference point as primarily being influenced by the electrostatic potential of the other atoms in the molecule. The electrostatic potential is long-range in nature, and therefore, it is expected that atomic basins quite distant from the reference point may bear upon the density. Some atoms act as sinks rather than sources; that is, the overall electrostatic pressure from within their atomic basins serves to remove rather than contribute density to $\rho(\mathbf{r})$ at the reference point. A strongly delocalized SF is observed for weak H-bonds,[63] where the source contributions are also primarily electrostatic in origin.

On the other hand, there are SF plots of a generally different form, as typified by Figure 9e where the reference point has been positioned at the bcp between O(2) and N(2) in the nitrate anion. In this case, the SF is highly localized, with the two atoms directly involved in the bcp contributing 88% of the charge density $\rho(\mathbf{r})$, whereas the remaining O(3) and O(4) atoms of the nitrate ion contribute 10.6%, that is, virtually all the remaining density. We take this as an indicator of the essentially shared (i.e., covalent) nature of the charge density at this bcp, arising primarily from the two atoms involved in the bcp, and with some indication of π-delocalization within the nitrate anion. The plots for reference points positioned at the Cu-ligator bcp's show a combination of these features. Figure 9b shows the plot for the Cu1−O1 bcp, where the two atoms directly involved contribute 71.7% of the density at $\rho(\mathbf{r})$, indicative of a substantial shared interaction. The remainder is built from smaller contributions, some of them from quite distant atoms. These delocalized contributions may indicate that there is a noticeable electrostatic (ionic) component of the Cu1−O1 bond. A similar situation pertains to the Cu1−O2 bond (64% contribution from the two atoms) and the Cu1−N1 bond (65.6% contribution from the two atoms). The primarily electrostatic nature of the bond to the pendant ligand, Cu1−O3′, is demonstrated by the highly delocalized SF. In this instance, the Cu1 center actually acts as sink (−4.6%) for $\rho(\mathbf{r})$, as do the ligator atoms N1 (−6.6%) and O2(−4.0%).

The SF for the weak intermolcular interactions between the binuclear complex and the pendant anions, observed in the molecular graphs, also displays the features of a primarily electrostatic interaction, see Figure 9h. Here, the very large negative and positive percentage contributions are possibly

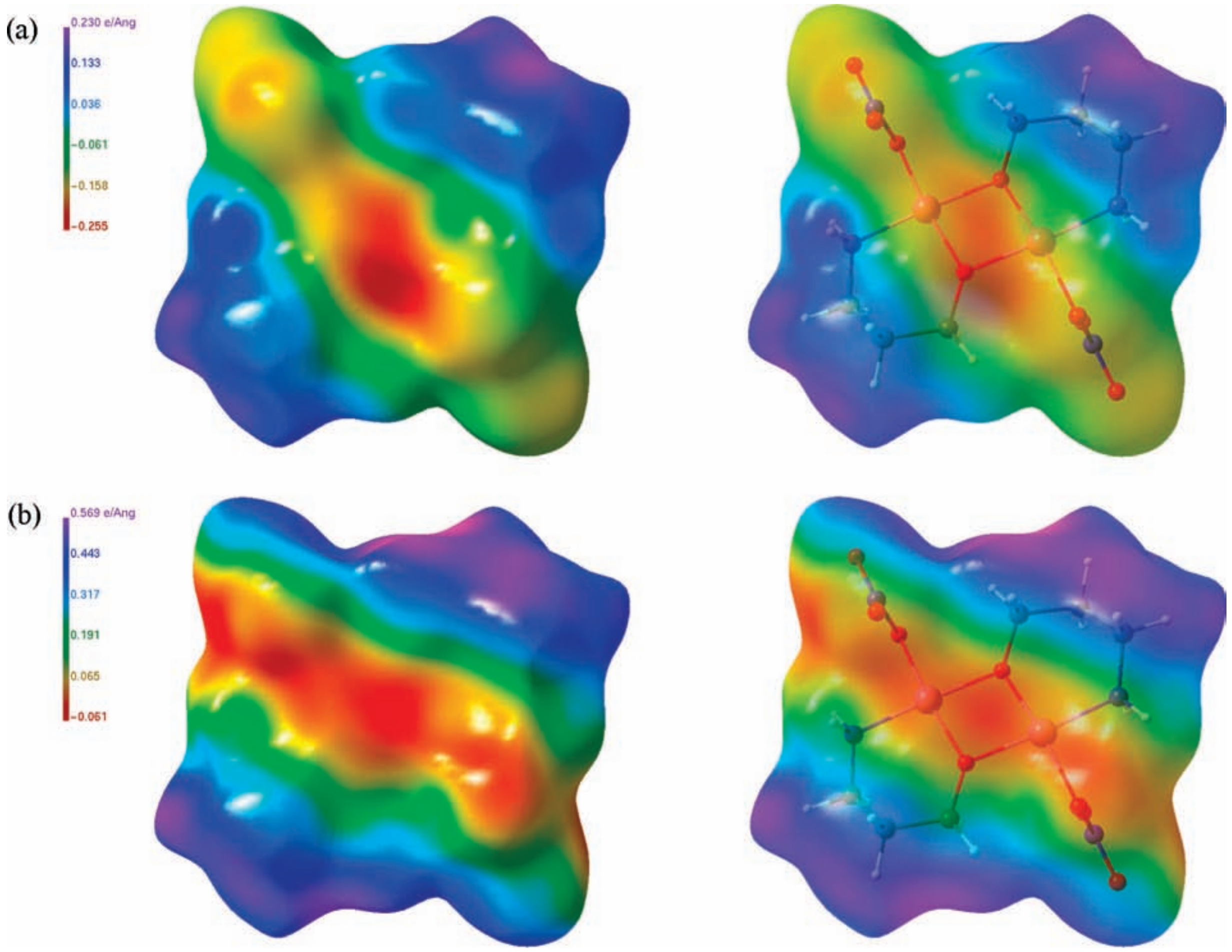

Figure 7. Experimental electrostatic potential $\phi(\mathbf{r})$ mapped onto the Hirshfeld surface of complex **2**; (a) $\phi(\mathbf{r})$ calculated for the isolated molecule and (b) $\phi(\mathbf{r})$ calculated for the molecule in the crystal. The left-hand view shows the solid surface, and the right-hand view shows the semitransparent surface displaying the molecular disposition.

artifacts of the integration errors, and the SF should be regarded as qualitative at best. The relative accuracy of reconstruction of $\rho(\mathbf{r})$ from the summation of atomic sources may be gauged by the quantity ER($\mathbf{r}$), defined[63a] as follows

$$\mathrm{ER}(\mathbf{r}) = 100 \times |\rho(\mathbf{r}) - \sum_{\Omega} S(\mathbf{r}, \Omega)| / \rho(\mathbf{r})$$

ER($\mathbf{r}$) is typically ~1% or less for the strong covalent interactions, where $\rho(\mathbf{r}_\mathbf{b}) \geq 0.2$ eÅ.$^{-3}$ Much higher values of ER($\mathbf{r}$) are observed for those reference points with very low values of $\rho(\mathbf{r})$ because of the higher percentage errors incurred in reconstructing $\rho(\mathbf{r})$ through the SF summation.[65] Although, in principle, the SF is obtainable from the experimental density, because of the computational expense, we have only integrated the atoms in the asymmetric units of **1**−**3**. This does not allow the complete determination of the experimental SF.

Finally, it should be stressed that covalent bonding delocalization can also lead to a rather delocalized SF, as has been found[26b] for instance in Fe(TMM)(CO)$_3$. In this case, the SF for reference points lying between the Fe atom and the TMM ligand is quite delocalized, with positive contributions coming from all atomic basins. The presence of basins which are significant sinks seems to be a marker of the importance of an electrostatic component, as discussed for H-bonds.[63] However, the interpretation of the SF in larger molecules is still in its infancy, and the study of further examples should clarify the matter. The interested reader is directed to more detailed discussions by Gatti et al.[64]

d-Orbital Populations and Atomic Charges. In the approximation of low covalency and low s−d mixing (not fully adhered to in our case), the d-orbital populations may be obtained from the multipole populations by the method of Coppens et al.[67] These populations are listed in Table 6. The partially occupied magnetic orbital is, as expected, the $d_{x^2-y^2}$ orbital.[68] Consequently, the present results provide direct experimental evidence in keeping with the commonly accepted superexchange mechanism[3] of magnetic coupling between the Cu(II) centers, which proceeds by the overlap of metal $d_{x^2-y^2}$ orbitals and p orbitals on the bridging O atoms. For a Cu(II) ion in an ideal D_{4h} Jahn−Teller distorted environment, the $(e_g)^4(b_{2g})^2(a_{1g})^2(b_{1g})^1$ electron configuration results in 11.1% occupation of the $d_{x^2-y^2}$ orbital and 22.2% for the remainder. In all our refinements, the population of the $d_{x^2-y^2}$ orbital is slightly higher, consistent with the presence of some covalent bonding with the basal ligator atoms, especially the N atom. A similar conclusion regarding the d-orbital populations of the Cu(II) ions in the layer compound [Cu$_2$(OH)$_3$(NO$_3$)] was reached by Lecomte et al.[9a]

The idea of local charges on atomic centers in molecules, though of profound interest to chemists, does not have a sound physical basis. Many partitioning schemes are possible, both in real space and Hilbert space, leading to a multitude of differing definitions of atomic charge.[69] Possibly the most rigorous definition comes from QTAIM,[6] with the space-partitioning by interatomic surfaces.[70] We quote in Table 7 the experimental and theoretical QTAIM charges and the integrated

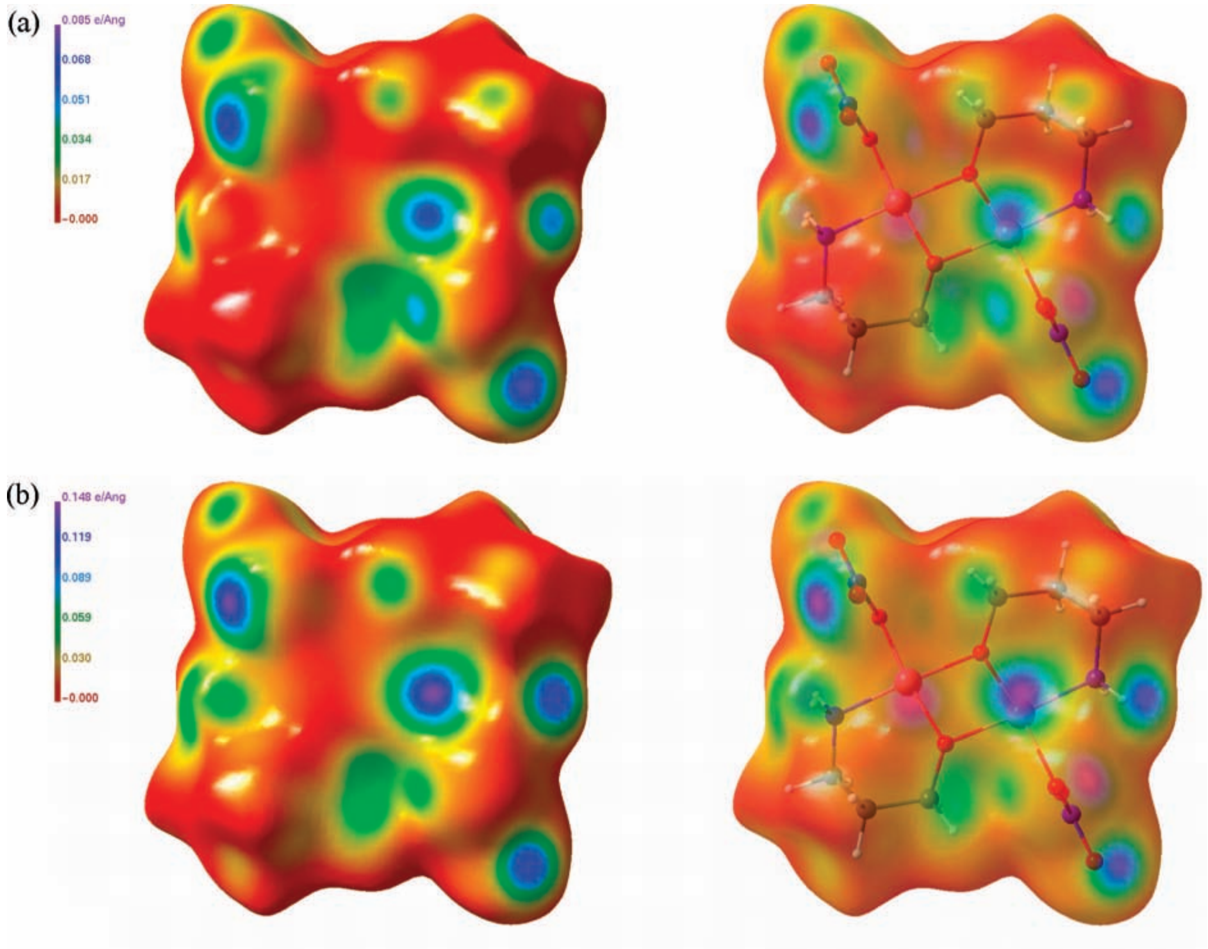

Figure 8. Experimental charge density $\rho(\mathbf{r})$ mapped onto the Hirshfeld surface of complex **2**; (a) $\rho(\mathbf{r})$ calculated for the isolated molecule and (b) $\rho(\mathbf{r})$ calculated for the molecule in the crystal. The left-hand view shows the solid surface, and the right-hand view shows the semitransparent surface displaying the molecular disposition.

TABLE 5: Integrated Interatomic Surface Densities $\oint_{A\cap B}$ $\rho(\mathbf{r})$ (e Å^{-1})

Surface (A-B)	1	2	3
Cu−O1	1.11	1.13	1.23
Cu−O1^{i}	1.22	1.21	1.19
Cu−O2	1.04	1.43	1.42
Cu−N1	1.30	1.34	1.32
Cu−O3^{ii}	0.42	0.63	0.49

TABLE 6: Experimentally Derived d-Orbital Populations

compound	d_{z^2}	d_{xz}	d_{yz}	$d_{x^2-y^2}$	d_{xy}	total
1(APEX II)	2.06(4)	1.86(4)	2.19(4)	1.17(4)	2.01(4)	9.29
1(KappaCCD)	1.97(4)	1.99(4)	2.13(4)	1.38(4)	2.08(4)	9.55
2	2.09(2)	2.24(2)	2.09(2)	1.57(2)	2.16(2)	10.15
3	2.13(2)	2.08(2)	2.30(2)	1.58(2)	2.13(2)	10.20

experimental Stockholder charges, partitioned according to the Hirshfeld method.[61] It is clear that (a) the Stockholder and QTAIM atomic charges are quite different, and the former are seemingly arbitrary and do not follow chemical intuition, (b) both charges are quite sensitive to the multipole model, insofar as the values obtained for complex **1** from the APEX II and KappaCCD refinements differ significantly, and (c) the experimental and theoretical QTAIM Cu charges do not agree well. However, the theoretical QTAIM charge on the Cu atom of ∼+1.2 is quite consistent in all three complexes and seems chemically reasonable, as do the corresponding charges for the other atoms (insofar as they follow from expectations based upon electro-negativity). Finally, we note that in three independent charge density studies on Cu(II) coordination complexes, the reported Ω(Cu) values vary from +0.22[15d] to +1.56[9c] to +1.9.[15a] This wide variation is undoubtedly in part due to the ambiguity of the experimental charge for transition metals mentioned above.

Atomic Graph of the Copper Atom. The polarization of the charge density around an atom upon formation of chemical bonds is very informative,[6] and its importance in experimental charge density analyses has been particularly emphasized by Scherer and co-workers.[40,71] The redistribution of charge is most simply described in terms of the critical points in the Laplacian of the density $\nabla^2\rho(\mathbf{r})$ in the valence shell charge concentration (VSCC), also termed the atomic graph. For transition metal atoms in approximate octahedral coordination, a classic cuboidal [8,12,6] atomic graph with O_h symmetry is almost always observed.[52a,c,72,73] This has eight charge concentrations maximally avoiding the ligator atom positions, as expected from simple ligand field theory. The six charge depletions in this graph face the ligator atoms, providing a key-and-lock rationalization for the bonding in coordination complexes.[52c]

In the case of complexes **1**−**3**, however, the severe Jahn−Teller distortion results in an atomic graph with approximate D_{4h} symmetry. We discuss here in detail the results obtained for the nitrate complex **2**, though similar observations apply to the other complexes. The atomic graph for the Cu(II) ion, obtained from topological analysis of the gas-phase DFT density (the

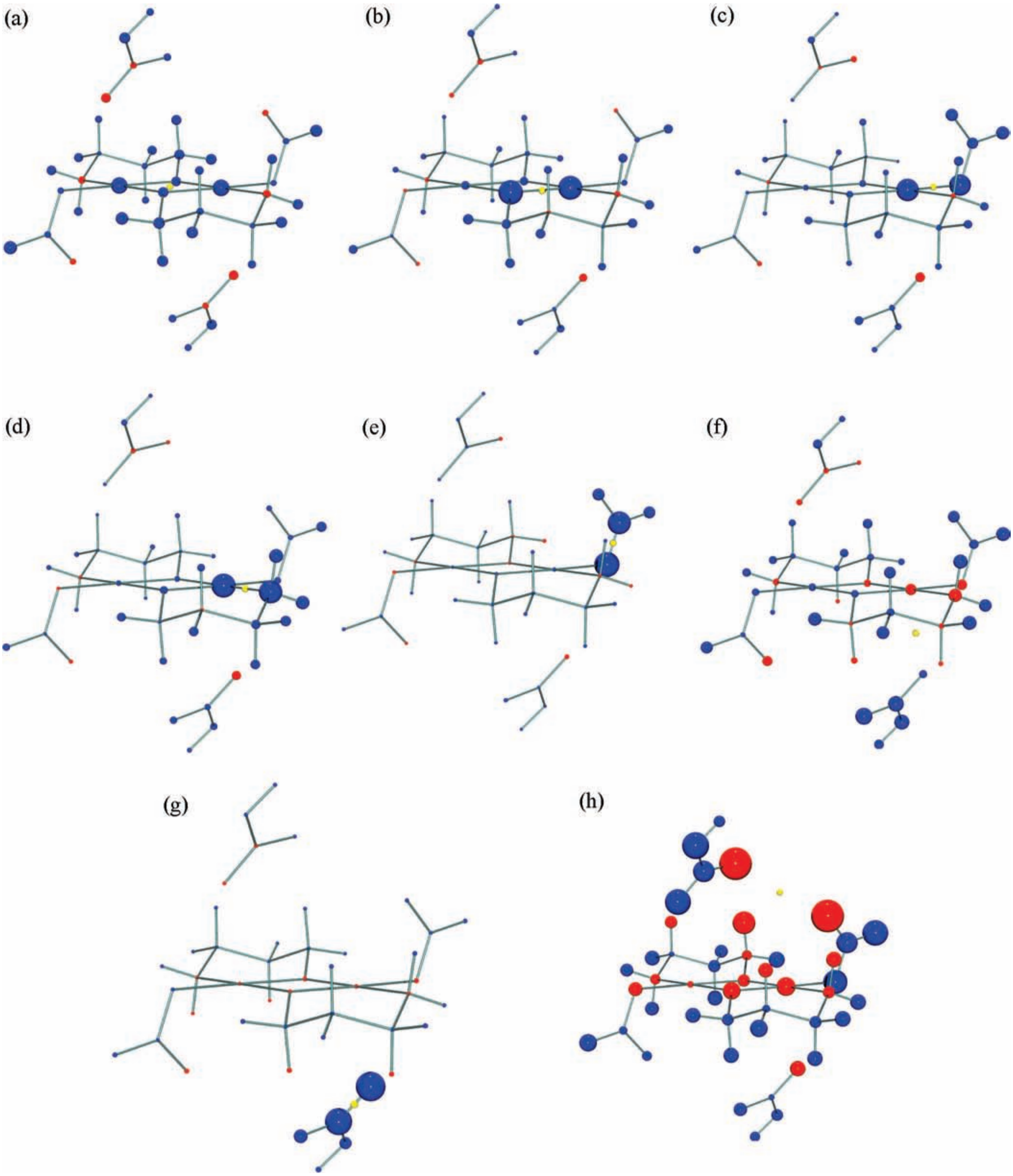

Figure 9. Integrated source function in complex **2**, with the reference points at (a) the (3,+1) rcp betwen the Cu centers, (b) the Cu1−O1 bcp, (c) the Cu1−O2 bcp, (d) the Cu1−N1 bcp, (e) the O2−N2 bcp, (f) the Cu1−O3^{ii} bcp, (g) the N2^{ii}−O3^{ii} bcp, and (h) the O3−O4^{iii} bcp. The volume of the spheres on the atomic centers are proportional to the percentage contributions from the requisite atomic basins; positive contributions (sources) are shown as blue spheres, and negative contributions (sinks) are shown as red spheres. The rerefence points are shown as yellow spheres.

reference graph), is shown in Figure 10a, and the mean values of $\rho(\mathbf{r})$ and $\nabla^2\rho(\mathbf{r})$ for each cp type are listed in Table 8. A topologically identical graph was obtained from the periodic CRYSTAL06 DFT density projected into atom centered multipoles, though the axial (3,+1) depletion cp's were slightly closer to the nucleus than the basal (3,+1) depletion cp's and hence have different properties (Table 7). There are four (3,−3) cp's of charge concentrations in $-\nabla^2\rho(\mathbf{r})$ localized in the basal plane containing the four strongly coordinated ligator atoms. These charge concentration cp's maximally avoid these ligator atoms, as expected from simple ligand-field theory. There are also six (3,+1) cp's associated with the charge depletions in

TABLE 7: Integrated Atomic Charges[a]

1	2	3
	Cu1	
+0.457 (+0.313)	−0.160	−0.283
+1.125 (+0.938)	+0.389	+0.322
+1.166	*+1.191*	*+1.202*
	O1	
−0.327 (−0.246)	−0.253	−0.391
−1.038 (−0.901)	−0.855	−1.036
−1.098	*−1.094*	*−1.101*
	O2	
−0.256 (−0.271)	−0.146	−0.318
−0.593 (−0.614)	−0.413	−0.969
−0.621	*−0.599*	*−1.164*
	O3	
−0.217 (−0.180)	−0.265	−0.313
−0.683 (−0.505)	−0.517	−1.004
−0.565	*−0.544*	*−1.206*
	O4/H4	
	−0.200	+0.161
	−0.354	+0.199
	−0.461	*−0.001*
	N1	
−0.059 (−0.137)	−0.174	−0.229
−0.806 (−0.779)	−0.987	−0.892
−0.928	*−0.944*	*−0.927*
	N2/C4	
+0.029 (+0.042)	+0.201	+0.231
+0.573 (+0.462)	+0.667	+1.320
+0.439	*+0.803*	*+1.596*
	C1	
+0.113 (+0.026)	−0.006	+0.098
+0.537 (+0.403)	+0.331	+0.493
+0.535	*+0.529*	*+0.562*
	C2	
−0.140 (−0.117)	−0.069	+0.142
−0.126 (−0.045)	+0.021	+0.185
+0.075	*+0.075*	*+0.073*
	C3	
−0.043 (+0.013)	+0.085	+0.091
+0.333 (+0.269)	+0.350	+0.382
+0.322	*+0.326*	*+0.327*

[a] Top line, Stockholder charges from experimental refinement; second line, Bader charges Ω(A) from experimental refinement; third line, Bader charges Ω(A) from DFT wavefunctions. For complex **1**, the values are those from APEX II refinement, with corresponding values from KappaCCD refinement in parentheses.

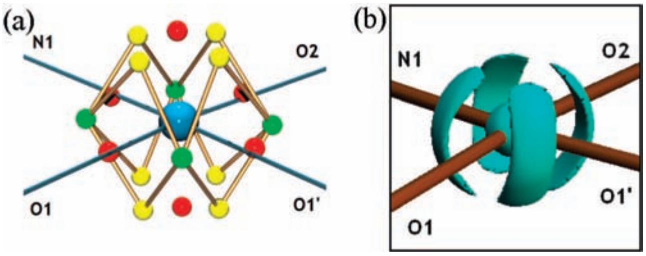

Figure 10. (a) Atomic graph of the Cu atom in complex **2**. Color coding: (3,−3) charge concentration cp's are shown in green, (3,−1) saddle-point cp's are shown in yellow, and (3,+1) charge depletions are shown in red. (b) Isosurface (−1700 e Å^{-5}) of the experimental Laplacian $\nabla^2\rho(\mathbf{r})$ around the Cu atom in complex **2**.

TABLE 8: Critical Points in the Laplacian of ρ in the VSCC of the Cu Atom[a]

$\rho(\mathbf{r})$ (eÅ^{-3})	$L(\mathbf{r}) \equiv -\nabla^2\rho(\mathbf{r})$ (eÅ^{-5})	distance $\mathbf{r}$ (Å)
	(3,−3)	
42.69	1981.2	0.281
45.16	2233.0	0.275
47.8	2290.0	0.274
	(3, −1)	
40.45	1449.1	0.286
42.35	1614.3	0.281
45.7	1782.6	0.278
	(3,+1)	
36.60	845.2	0.293
36.5,41.6	687.7,1431.3	0.291,0.283
39.1,41.3	919.5, 1072.7	0.285

[a] Data for complex **2**; top line from gas-phase DFT density, second line from periodic DFT density, third line from experimental multipole model.

the VSCC and which lie approximately along the octahedral Cu(II)−ligator atom vectors.

The experimental atomic graph obtained for **2** (and indeed for the other complexes) is highly dependent on the multipole model used for the Cu atom. The difficulties in reproducing theoretical atomic graphs from experimentally refined multipole models has been discussed previously.[73] To illustrate the situation, four different multipole models were examined, with increasing restrictions on the allowed (nonzero) populations on the Cu centers. Because only the even-order multipoles may model pure d-electron density, the odd-order multipoles are primarily used to model the metal sp- and dp-hybridized and the diffuse ligand-centered density. In multipole model (MM) 1, all multipole populations ($l = 0-4$) were allowed to refine, giving the most flexible model. In MM2, the same conditions as for MM1 applied, except that all populations with $|P_{nm}| \leq 3\sigma(P_{nm})$ were zeroed and not further refined. In MM3, only the even-order multipoles were refined, whereas in MM4, only that subset complying with exact D_{4h} symmetry (P_{20}, P_{40}, and P_{44}) were refined. The quadrupole (P_{2m}) and the hexadecapole (P_{4m}) populations for these refinements are listed in Tables S18 and S19 in the Supporting Information, and the atomic graphs are shown in Figure S13 in Supporting Information. In general, it is clear that the populations of all multipoles forbidden under strict D_{4h} symmetry are quite small. Nevertheless, it is also clear that the inclusion of these small populations leads to significant differences in the atomic graphs. It is important to stress here that the discrepancies we observe cannot be attributed to any deficiencies in the standard Hansen−Coppens multipole model. Refinement against the synthetic structure factors obtained from the CRYSTAL06 periodic wave function, even by using the most flexible MM1, gave an atomic graph of D_{4h} symmetry, identical to the reference graph. For all complexes, apart from **1** (APEX-II data), the least-squares fit is only marginally worse for the severely restrictive MM4 compared with the completely unrestricted MM1. We conclude that the experimental deformation density around the Cu(II) ions in complexes **1**−**3** may be reasonably approximated by D_{4h} symmetry.

In fact, the main differences between the experimental and reference (Figure 10a) graphs arise in the positions of the (3,−3) charge concentration cp's, which are found to lie either within the basal plane or above or below it. The underlying reason is evident from the isosurface plot of the experimental Laplacian shown in Figure 10b, which reveals that the charge concentrations from the d orbitals are highly elongated along the unique axial direction. These may be contrasted with recent work by Scherer et al.[40] on $Sc_3[M(C_2)_2]$ (M = Fe,Co), where the charge concentrations for the Fe and Co atoms (which have the same, approximately square-planar, coordination geometry as the Cu(II) ions in **1**−**3**) are much more strongly localized in the basal plane. The choice of which multipoles to

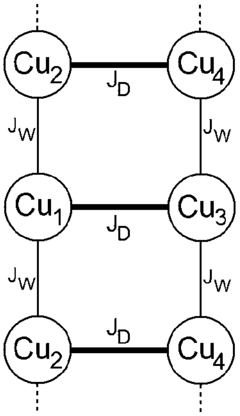

Figure 11. Magnetic connectivity of the four Cu sites in the unit cell of complexes **2** and **3**.

include in the experimental model is a clearly a delicate one and cannot be judged merely on the criterion of the best least-squares fit. Moreover, enforcing D_{4h} symmetry by imposing a restrictive multipole model suffers from the philosophical problem that one is using a priori knowledge to fit a known theoretical result. In fact, even when using the restrictive MM4, it was not possible to reproduce the theoretical atomic graph for Cu from the experimental data for the formate complex **3**. The atomic graph obtained (Figure S14 in the Supporting Information) naturally complies with D_{4h} symmetry but has the basal (3,−3) charge concentration cp's split into two, with each pair linked by a saddle-point (3,−1) cp. We are only aware of one other report[15a] of the determination of the experimental atomic graph for a Cu(II) ion—this was in a ciproflavin complex, where six charge concentrations were observed.

Relative Strengths of Magnetic Couplings. Further solid-state calculations performed by using the CRYSTAL06[48] code were undertaken for the exchange coupling strengths in the more tractable unit cells of complexes **2** and **3**. The nearest-neighbor (nn) Cu−Cu separations of 2.96 and 2.98 Å, respectively, are associated with strong intradimer couplings (J_D), whereas the two next-nearest-neighbor (nnn) separations of 4.42 and 4.57 Å, respectively, are associated with weaker interdimer interactions (J_W). Figure 11 depicts the magnetic connectivity of the four Cu sites in the crystallographic cell. As in related studies,[74] the magnetic energy of the crystal is expressed in terms of an Ising Hamiltonian of the form

$$\hat{H}^{\text{spin}} = \hat{H}_0 + \frac{J_D}{2}\sum_{ij}^{nn} S_i S_j + \frac{J_W}{2}\sum_{ij}^{nnn} S_i S_j$$

where $S = \pm(1/2)\hbar$ is the spin borne by each Cu(II) ion and indices i and j run over all Cu(II) sites. Positive J values favor an antiferromagnetic (AF) spin alignment within this sign convention. We consider the ferromagnetic (FM), AF type-1 (AF_1) and AF type-2 (AF_2) states with Cu 1−4 spin alignments as shown below, obtaining energies per Cu site as follows

$$E_{FM}[1\uparrow 2\uparrow 3\uparrow 4\uparrow] = E_0 + \frac{J_D}{2}S(S+1) + J_W S(S+1)$$

$$E_{AF_1}[1\uparrow 2\uparrow 3\downarrow 4\downarrow] = E_0 - \frac{J_D}{2}S(S+1) + J_W S(S+1)$$

$$E_{AF_2}[1\uparrow 2\downarrow 3\downarrow 4\uparrow] = E_0 - \frac{J_D}{2}S(S+1) - J_W S(S+1)$$

where E_0 is the energy of the hypothetical nonmagnetic lattice. Finally, we compute the coupling constants from the differences in the energies of the states,

$$J_D = \frac{E_{FM} - E_{AF_1}}{S(S+1)} \text{ and } J_W = \frac{E_{AF_1} - E_{AF_2}}{2S(S+1)}$$

First, we note that all of the calculations yield AF_2 ground magnetic states, indicative of AF intra- and interdimer interactions. The AF_1 and FM states are 0.324 and 739.5 μE_h per Cu site higher in energy, respectively, in **2** and 1.063 and 535.9 μE_h per Cu site higher in energy, respectively, in **3.** Substitution of these values into the above expressions yields J_D and J_W values of +216.314 and +0.047 cm^{-1}, respectively, in **2** and of +156.513 and +0.156 cm^{-1}, respectively, in **3**. The low ratios J_W/J_D of approximately 2.2×10^{-4} and 9.9×10^{-4}, respectively, confirms that the magnetic structures of complexes **2** and **3** may be reasonably represented as an array of isolated spin-1/2 dimers. Our computed triplet−singlet splittings $2J_D S(S+1)$ of 324.5 and 244.8 cm^{-1} for **2** and **3**, respectively, compare reasonably well with the experimental values of 387 and 282 cm^{-1}, respectively, obtained from fits of the Bleaney−Bowers equation to the magnetic susceptibility data.[12a] The quality of agreement is particularly gratifying given that no attempt was made to optimize the crystal structures; we note in particular that the computed ratio J_D(**2**)/J_D(**3**) of 1.33 is in excellent agreement with experimental value of 1.37. As recently pointed out by Lecomte et al.,[9b] magnetic exchange in the crystal phase may also be mediated by intermolecular H-bonds, such as the A−C interaction in **3**, shown in Figure 2. Unfortunately, because of the intractable computational size of the problem, we were not able to quantitatively assess this interaction pathway in complexes **2** and **3**.

The difference in magnetic coupling observed in complexes **2** and **3** is clearly real and significant. Complexes **1**−**3** possess similar θ angles of ~100°, for which a value for $-2J$ of ~200 cm^{-1} is predicted on the basis of the Hatfield, Hodgson et al.[2a] correlation. Moreover, the τ angle is also very similar for all three complexes. It seems likely therefore that the deviation of the Cu coordination geometry from planarity is the most probable cause[5] of the differing $-2J$ values observed in complexes **2** and **3** by both theory and experiment. The degree of distortion away from perfect D_{4h} symmetry[75a] may be quantified by the continuous shape measure (CSM) of Pinsky and Avnir.[76] By using the SHAPE software,[75b] we compute values for the CSM index $S(D_{4h})$ of 0.485, 0.396, and 0.920 for **1**−**3**, respectively. Although the $-2J$ values do indeed show some correlation with the $S(D_{4h})$ indices, the trend is clearly not linear.

The spin density obtained from the gas-phase DFT calculation on the ground state, broken symmetry singlet in compound **2** is shown in Figure 12, whereas the corresponding Mulliken atomic spin densities are presented in the Supporting Information. Figure 11 clearly shows intradimer coupling proceeds via the delocalization[77] of Cu(II) spin density into the σ-bonding p-orbitals of the bridging O atoms. The experimental determination of spin density by spin polarized neutron diffraction (PND)[78] has been reported for a number of binuclear complexes. As far as we are aware, there is only one such study on hydroxy/alkoxy bridged Cu(II) complexes, by Figgis et al.,[79] on $Cu_2(\mu\text{-}OH)_2(bpy)_2(OH_2)(SO_4)$, which is ferro- rather than antiferromagnetically coupled. Gillon and co-workers[80] have reported PND studies on several binuclear complexes containing Cu(II), though antiferromagnetic coupling was only observed for the heterobimetallic[80c−e] complexes. The spin distribution in **2** shown in Figure 11 for the Cu(II) ions is the expected[77b] one for a d^9 ion.

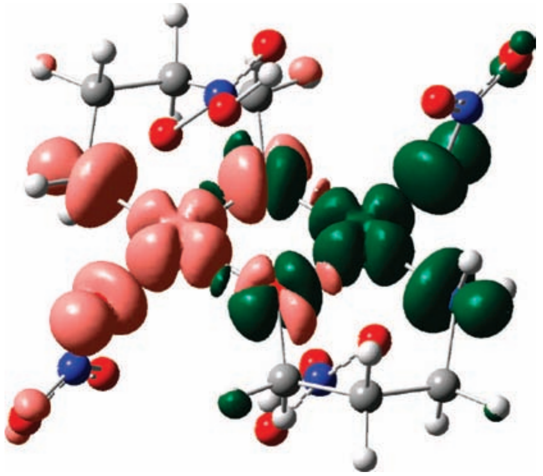

Figure 12. Representation of the spin density in the broken symmetry singlet state of compound **2** (α in green, β in pink, isosurface at 1.6×10^{-3} e Å^{-3}) from the DFT calculation.

Conclusions

The topological analyses of the experimental and theoretical densities for **1**−**3** are in excellent agreement and demonstrate that the Cu−O and Cu−N bonding in the primary coordination sphere has a strong covalent component but that the weak secondary Cu···O interactions are primarily electrostatic in nature. Only in complex **1** is there any evidence for bidentate coordination of the L$^-$ anion. Despite some deficiency in the quality of the experimental data for **1** (APEX II data), there are no consistent discrepancies in the primary topological indicators between the two data sets. The absence of a direct Cu···Cu interaction, coupled with the ring structure of the $Cu_2(\mu\text{-}O)_2$ unit and the d-orbital populations provides experimental evidence for the dominance of a superexchange mechanism through the bridging O atoms. The very low δ(Cu−Cu′) delocalization index corroborates this interpretation. In this first investigation of the SF in a coordination complex, it is shown that this topological indicator provides insight into the relative electrostatic and covalent contributions to the chemical bonds. As we have previously demonstrated, the topology of the charge density in the valence shell charge concentration of the transition metal is highly sensitive to the multipole model used for that metal, and experimental determinations should be interpreted with caution. Periodic DFT calculations on **2** and **3** show the intradimer magnetic coupling proceeds via spin delocalization onto the bridging O atoms. The magnetic coupling between dimers through the L$^-$ anionic bridges is shown to be insignificant, and the computed values of the intradimer magnetic coupling constants $-2J$ compare well with previously determined experimental values.

Acknowledgment. The work in Glasgow was supported by the University of Glasgow and the EPSRC under Grant GR/M91433 for the purchase of a KappaCCD diffractometer and under Grants GR/T21615 and GR/T21608 for PDRA funding for D.S.M. The work in Jyväskylä was supported by the Academy of Finland (R.S.). We also thank Professor John McGrady for helpful discussions regarding broken symmetry calculations and for computing time on the Computational Chemistry Cluster.

Supporting Information Available: Final refined parameters, observed and calculated structure factors in CIF format for the multipole refinements; supplementary figures (22) of plots of scale factors versus (sin θ)/λ, residual density maps and distribution plots, molecular graphs of **2**, crystal packing diagrams, atomic graphs for **2**, and plots of $\rho(\mathbf{r})$ and $\phi(\mathbf{r})$ on Hirshfeld surfaces; supplementary tables (19) of residual density peaks, Mulliken atomic spin densities, full critical point and source function contribution data, multipole populations for Cu with different models. This material is available free of charge via the Internet at http://pubs.acs.org.

References and Notes

(1) (a) Kahn, O. *Molecular Magnetism*; VCH Publishers: New York, 1993. (b) *Molecular Magnetism*; Itoh, K., Kinoshita, M., Eds.; Gordon and Breach Science Publisher: Amsterdam, Netherlands, 2000. (c) *Molecular Magnetism: From Molecular Assemblies to the Devices*; Coronado, E., Delhaès, P., Gatteschi, D., Miller, J. S., Eds.; Nato ASI Series E, Applied Sciences, Kluwer Academic Publisher: Dordrecht, Netherlands, 1996; *Vol. 321*. (d) *Magnetism: Molecules to Materials I: Models and Experiments and Magnetism: Molecules to Materials II: Molecule-Based Materials and Experiments*; Miller, J. S., Drillon, M., Eds.; Wiley-VCH: New York, NY, 2001. (e) *Molecular Magnets: Recent Highlights*; Linert, W., Verdaguer, M., Eds.; Springer-Verlag: Vienna, Austria, 2003.

(2) (a) Crawford, V. H.; Richardson, H. W.; Wasson, J. R.; Hodgson, D. J.; Hatfield, W. E. *Inorg. Chem.* **1976**, *15*, 2107. (b) Merz, L.; Haase, W. *J. Chem. Soc., Dalton Trans.* **1980**, 875. (c) Thompson, L. K.; Mandal, S. K.; Tandon, S. S.; Bridson, J. N.; Park, M. K. *Inorg. Chem.* **1996**, *35*, 3117.

(3) (a) Hay, P. J.; Thibeault, J. C.; Hoffmann, R. *J. Am. Chem. Soc.* **1975**, *97*, 4884. (b) Kahn, O. *Inorg. Chim. Acta* **1982**, *62*, 3.

(4) (a) Anderson, P. W. *Solid State Phys.* **1963**, *14*, 99. (b) Goodenough, J. B. *Magnetism and the Chemical Bond*; Interscience, New York, 1963. (c) Goodenough, J. B. *Phys. Rev.* **1955**, *100*, 504. (d) Goodenough, J. B. *Phys. Chem. Solids* **1958**, *6*, 287. (e) Kanamori, J. *Phys. Chem. Solids* **1959**, *10*, 87.

(5) (a) Asthheimer, H.; Hasse, W. *J. Chem. Phys.* **1986**, *85*, 1427. (b) Handa, M.; Koga, N.; Kida, S. *Bull. Chem. Soc. Jpn.* **1988**, *61*, 3853. (c) Ruiz, E.; Alemany, P.; Alvarez, S.; Cano, J. *J. Am. Chem. Soc.* **1997**, *119*, 1297. (d) Ruiz, E.; Alemany, P.; Alvarez, S.; Cano, J. *Inorg. Chem.* **1997**, *36*, 3683. (e) Hu, H.; Liu, Y.; Zhang, D.; Liu, C. *J. Mol. Struct (Theochem)* **2001**, *546*, 73.

(6) (a) Bader, R. F. W. *Atoms in Molecules: A Quantum Theory; International Series of Monographs in Chemistry 2*; Oxford University Press: Oxford, 1990. (b) Popelier, P. *Atoms in Molecules: An Introduction*; Prentice Hall, Harlow, 2000. (c) *The Quantum Theory of Atoms in Molecules: From Solid State to DNA and Drug Design* Matta, C. F., Boyd, R. J., Eds.;Wiley-VCH, Weinheim, 2007.

(7) (a) Coppens, P. *X-ray Charge Densities and Chemical Bonding*; Oxford Science Publications: Oxford, 1997. (b) Tsirelson, V. G.; Ozerov, R. P. *Electron Density and Bonding in Crystals*; Institute of Physics Publishing: Bristol, 1996. (c) Coppens, P. *Acta Crystallogr., Sect. A* **1998**, *54*, 779. (d) Koritsanszky, T. S.; Coppens, P. *Chem. Rev.* **2001**, *101*, 1583.

(8) (a) Bertini, L.; Cargnoni, F.; Gatti, C. *Theor. Chem. Acc.* **2007**, *117*, 847. (b) Coppens, P.; Volkov, A. *Acta Crystallogr., Sect. A.* **2004**, *60*, 357.

(9) (a) Pilet, S.; Souhassou, M.; Lecomte, C.; Rabu, P.; Drillon, M.; Massabrio, C. *Phys. Rev.* **2006**, *B73*, 115116. (b) Pilet, S.; Souhassou, M.; Lecomte, C. *Acta Crystallogr., Sect. A.* **2004**, *60*, 455. (c) Pilet, S.; Souhassou, M.; Mathoniére, C.; Lecomte, C. *J. Am. Chem. Soc.* **2004**, *126*, 1219. (d) Yasui, M.; Takayama, R.; Akiyama, N.; Hashizume, D.; Iwasaki, F. *Mol. Cryst. Liq. Cryst.* **2002**, *376*, 519. (e) Poulsen, R. D.; Bentien, A.; Graber, T.; Iversen, B. B. *Acta Crystallogr., Sect. A* **2004**, *60*, 382–389.

(10) (a) Bader, R. F. W. *J. Phys. Chem. A* **1998**, *102*, 7314. (b) Abramov, Y. A. *J. Phys. Chem. A* **1997**, *101*, 5725. (c) Haaland, A.; Shorokhov, D. J.; Tverdova, N. J. *Chem. Eur. J.* **2004**, *10*, 4416. (d) Cioslowski, J.; Mixon, S. T.; Edwards, W. D. *J. Am. Chem. Soc.* **1991**, *113*, 1083. (e) Cioslowski, J.; Mixon, S. T. *Can. J. Chem.* **1992**, *70*, 443. (f) Cioslowski, J.; Mixon, S. T. *J. Am. Chem. Soc.* **1995**, *114*, 4383. (g) Cioslowski, J.; Edgington, L.; Stefanov, B. B. *J. Am. Chem. Soc.* **1995**, *117*, 10381. (h) Bader, R. F. W.; Fang, D.-C. *J. Chem. Theory Comput.* **2005**, *1*, 403. (i) Matta, F.; Hernández-Trujillo, J.; Tang, T.-H.; Bader, R. F. W. *Chem. Eur. J.* **2003**, *9*, 1940. (j) Poater, J.; Solà, M.; Bickelhaupt, F. M. *Chem. Eur. J.* **2006**, *12*, 2889. (k) Bader, R. F. W. *Chem. Eur. J.* **2006**, *12*, 2896. (l) Poater, J.; Solà, M.; Bickelhaupt, F. M. *Chem. Eur. J.* **2006**, *12*, 2902.

(11) Pendás, M. A.; Francisco, E.; Blanco, M. A.; Gatti, C. *Chem. Eur. J.* **2007**, *13*, 9362.

(12) (a) Lindgren, T.; Sillanpää, R.; Rissanen, K.; Thompson, L. K.; O'Connor, C. J.; Van Albada, G. A.; Reedijk, J. *Inorg. Chim. Acta* **1990**, *171*, 95. (b) Sillanpää, R.; Lindgren, T.; Rissanen, K. *Inorg. Chim. Acta* **1987**, *134*, 233.

(13) Seppälä, P.; Colacio E.; Sillanpää, R. Unpublished results.

(14) Bleaney, B.; Bowers, K. D. *Proc. R. Soc. London* **1952**, *A214*, 451.

(15) (a) Overgaard, J.; Turel, I.; Hibbs, D. E. *J. Chem. Soc., Dalton Trans.* **2007**, 2171. (b) Kožíšek, Hansen, N. K.; Fuess, H. *Acta Crystallogr., Sect. B* **2002**, *58*, 463. (c) Yasui, M.; Ishikawa, Y.; Akiyama, N.; Ishida, T.; Nogami, T.; Iwasaki, F. *Acta Crystallogr., Sect. B* **2001**, *57*, 288. (d) Bytheway, I.; Figgis, B. N.; Sobolev, A. N. *J. Chem. Soc., Dalton Trans.* **2001**, 3825.

(16) (a) Ghermani, N.-E.; Lecomte, C.; Rapin, C.; Steinmetz, P.; Steinmetz, J.; Malaman, B. *Acta Crystallogr., Sect. B* **1994**, *50*, 157. (b) Figgis, B. N.; Iversen, B. B.; Larsen, F. K.; Reynolds, P. A. *Acta Crystallogr., Sect. B* **1993**, *49*, 794. (c) Maslen, E. N.; Watson, K. J.; Moore, F. H. *Acta Crystallogr., Sect. B* **1988**, *44*, 102. (d) Maslen, E. N.; Spadaccini, N.; Watson, K. J.; White, A. H. *Acta Crystallogr., Sect. B* **1986**, *42*, 430. (e) Varghese, J. N.; Maslen, E. N. *Acta Crystallogr., Sect B* **1985**, *41*, 184–190.

(17) *APEX2 v2.1−4* and *SAINT v7.34A*; Software Bruker AXS Inc.: Madison, Wisconsin, 2007.

(18) Coppens, P.; Leiserowitz, L.; Rabinovich, D. *Acta Crystallogr.* **1965**, *18*, 1035.

(19) Blessing, R. H. *Acta Crystallogr., Sect. A* **1995**, *51*, 33.

(20) Sheldrick, G. M. *SADABS version 2008/1*; University of Göttingen: Germany., 2008.

(21) Blessing, R. H. *J. Appl. Crystallogr.* **1997**, *30*, 421.

(22) Sheldrick, G. M. *Acta Crystallogr., Sect. A* **2008**, *64*, 112.

(23) Tables 4.2.4.2, 4.2.6.8, and6.1.1.4. *International Tables for Crystallography, Volume C Mathematical, Physical and Chemical Tables*; Kluwer: Dordrecht, 1995.

(24) Farrugia, L. J. *J. Appl. Crystallogr.* **1997**, *30*, 565.

(25) Farrugia, L. J. *J. Appl. Crystallogr.* **1999**, *32*, 837.

(26) (a) DENZOX−Program for processing Denzo x files; Blessing, R. H. 1997. (aa) Modified for KappaCCD data; Farrugia, L. J.; Muir, K. W. 2001. (b) Farrugia, L. J.; Evans, C.; Tegel, M. *J. Phys. Chem. A* **2006**, *110*, 7052.

(27) Otwinowski, Z.; Minor, W. Processing of X-ray Diffraction Data Collected in Oscillation Mode In *Methods in Enzymology, Volume 276: Macromolecular Crystallography, part A*; Carter C. W., Jr., Sweet, R. M., Eds.; Academic Press, 1997; pp 307−326.

(28) Hansen, N. K.; Coppens, P. *Acta Crystallogr., Sect. A* **1978**, *34*, 909.

(29) (a) XD2006−A Computer Program for Multipole Refinement, Topological Analysis of Charge Densities and Evaluation of Intermolecular Interaction Energies From Experimental or Theoretical Structure Factors. Volkov, A.; Macchi, P.; Farrugia, L. J.; Gatti, C.; Mallinson, P.; Richter, T.; Koritsanszky, T. 2006. (b) Hübschle, C. B.; Luger, P. *J. Appl. Crystallogr.* **2006**, *39*, 901. (c) Volkov, A.; King, H. F.; Coppens, P.; Farrugia, L. J. *Acta Crystallogr., Sect. A* **2006**, *62*, 400. (d) Volkov, A.; Koritsanszky, T.; Coppens, P. *Chem. Phys. Lett.* **2004**, *391*, 170.

(30) (a) Whitten, A. E.; Spackman, M. A. *Acta. Crystallogr., Sect. B* **2006**, *62*, 875. (b) Whitten, A. E.; Turner, P.; Klooster, W. T.; Piltz, R. O.; Spackman, M. A. *J. Phys. Chem. A.* **2006**, *110*, 8763. (c) Madsen, A. Ø.; Sørensen, H. S.; Flensburg, C.; Stewart, R. F.; Larsen, S. *Acta Crystallogr., Sect. A* **2004**, *60*, 550.

(31) (a) Madsen, A. Ø. *J. Apply. Cryst.* **2006**, *39*, 757. (b) SHADE server: http://shade.ki.ku.dk.

(32) Su, Z.; Coppens, P. *Acta Crystallogr., Sect A.* **1998**, *54*, 646.

(33) Bunge, C. F.; Barrientos, J. A.; Bunge, A. V. *At. Data Nucl. Data Tab.* **1993**, *53*, 113.

(34) Coppens, P. *Coord. Chem. Rev.* **1985**, *65*, 285.

(35) (a) Becker, P. J.; Coppens, P. *Acta Crystallogr., Sect. A* **1974**, *30*, 129. (b) Becker, P. J.; Coppens, P. *Acta Crystallogr., Sect. A* **1974**, *30*, 148. (c) Becker, P. J.; Coppens, P. *Acta Crystallogr., Sect. A* **1975**, *31*, 417.

(36) Hirshfeld, F. L. *Acta Crystallogr., Sect. A* **1976**, *32*, 239.

(37) Abramov, Y. A. *Acta Crystallogr., Sect. A* **1997**, *53*, 264.

(38) Gálvez, O.; Gómez, P. C.; Pacios, L. F. *Chem. Phys. Lett.* **2001**, *337*, 263.

(39) Meindl, K.; Henn, J. *Acta Crystallogr., Sect. A* **2008**, *64*, 404.

(40) Rohrmoser, B.; Eickerling, G.; Presnitz, M.; Scherer, W.; Eyert, W.; Hoffmann, R.-D.; Rodewald, U. C.; Vogt, C.; Põttgen, R. *J. Am. Chem. Soc.* **2007**, *129*, 9356–9365.

(41) Zhurov, V. I.; Zhurova, E. A.; Pinkerton, A. A. *J. Appl. Crystallogr.* **2008**, *41*, 340.

(42) Pinkerton, A. A. Unpublished observations (quoted in ref 30b).

(43) Frisch, M. J.; Trucks, G. W.; Schlegel, H. B.; Scuseria, G. E.; Robb, M. A.; Cheeseman, J. R.; Montgomery, J. A., Jr.; Vreven, T.; Kudin, K. N.; Burant, J. C.; Millam, J. M.; Iyengar, S. S.; Tomasi, J.; Barone, V.; Mennucci, B.; Cossi, M.; Scalmani, G.; Rega, N.; Petersson, G. A.; Nakatsuji, H.; Hada, M.; Ehara, M.; Toyota, K.; Fukuda, R.; Hasegawa, J.; Ishida, M.; Nakajima, T.; Honda, Y.; Kitao, O.; Nakai, H.; Klene, M.; Li, X.; Knox, J. E.; Hratchian, H. P.; Cross, J. B.; Bakken, V.; Adamo, C.; Jaramillo, J.; Gomperts, R.; Stratmann, R. E.; Yazyev, O.; Austin, A. J.; Cammi, R.; Pomelli, C.; Ochterski, J. W.; Ayala, P. Y.; Morokuma, K.; Voth, G. A.; Salvador, P.; Dannenberg, J. J.; Zakrzewski, V. G.; Dapprich, S.; Daniels, A. D.; Strain, M. C.; Farkas, O.; Malick, D. K.; Rabuck, A. D.; Raghavachari, K.; Foresman, J. B.; Ortiz, J. V.; Cui, Q.; Baboul, A. G.; Clifford, S.; Cioslowski, J.; Stefanov, B. B.; Liu, G.; Liashenko, A.; Piskorz, P.; Komaromi, I.; Martin, R. L.; Fox, D. J.; Keith, T.; Al-Laham, M. A.; Peng, C. Y.; Nanayakkara, A.; Challacombe, M.; Gill, P. M. W.; Johnson, B.; Chen, W.; Wong, M. W.; Gonzalez, C.; Pople, J. A. *Gaussian 03*, revision D.02; Gaussian, Inc.: Wallingford, CT, 2004.

(44) Basis sets were obtained from the Extensible Computational Chemistry Environment Basis Set Database, Version 02/25/04, as developed and distributed by the Molecular Science Computing Facility, Environmental and Molecular Sciences Laboratory which is part of the Pacific Northwest Laboratory, P.O. Box 999, Richland, Washington 99352, and funded by the U.S. Department of Energy. The Pacific Northwest Laboratory is a multi-program laboratory operated by Battelle Memorial Institute for the U.S. Department of Energy under Contract DE-AC06−76RLO 1830.

(45) Biegler-König, F. W.; Bader, R. F. W.; Tang, T.-H. *J. Comput. Chem.* **1982**, *3*, 317.

(46) Biegler-König, F. *J. Comput. Chem.* **2000**, *12*, 1040.

(47) Volkov, A. V. WFN2HKL - a parallellized program for calculation of static structure factors from electron densities represented with Gaussian- and Slater-type functions; Middle Tennessee State University, 2008.

(48) Dovesi, R.; Saunders, V. R.; Roetti, C.; Orlando, R.; Zicovich-Wilson, C. M.; Pascale, F.; Civalleri, B.; Doll, K.; Harrison, N. M.; Bush, I. J.; D'Arco, Ph.; Llunell, M. *CRYSTAL06 User's Manual*; University of Torino: Torino, 2006.

(49) Monkhorst, H. J.; Pack, J. D. *Phys. Rev. B* **1976**, *13*, 5188.

(50) Etter, M. C.; MacDonald, J. C.; Bernstein, J. *Acta Crystallogr., Sect. B* **1990**, *46*, 256.

(51) Bader, R. F. W.; Essen, H. *J Phys. Chem. A* **1984**, *80*, 1943.

(52) (a) Macchi, P.; Sironi, A. *Coord. Chem. Rev.* **2003**, *238*, 383, and refs therein. (b) Gatti, C. Z. *Kristallogr.* **2005**, *220*, 399, and refs therein. (c) Cortés-Guzman, F.; Bader, R. F. W. *Coord. Chem. Rev.* **2005**, *249*, 633.

(53) (a) Fradera, X.; Austen, M. A.; Bader, R. F.; W, *J. Phys Chem. A* **1999**, *103*, 304. (b) Ángyán, J. G.; Loos, M.; Mayer, I. *J. Phys. Chem.* **1994**, *98*, 5244. (c) for calculations of delocalization indices in open shell molecules see Fradera, X.; Solà., M. *J. Comput. Chem.* **2002**, *23*, 1347.

(54) Cremer, D.; Kraka, E. *Croat. Chem. Acta* **1984**, *57*, 1259.

(55) Eickerling, G.; Mastalerz, R.; Herz, V.; Scherer, W.; Himmel, H.-J.; Reiher, M. *J. Chem. Theory Comput.* **2007**, *3*, 2182–2197.

(56) The ellipticity ε of the charge density at the bcp is defined as λ_1/λ_2-1, where λ_1 and λ_2 are the smallest eigenvalues of the Hessian matrix.

(57) Farrugia, L. J.; Frampton, C. S.; Howard, J. A. K.; Mallinson, P. R.; Peacock, R. D.; Smith, G. T.; Stewart, B. *Acta Crystallogr., Sect. B* **2006**, *62*, 236.

(58) Espinosa, E.; Alkorta, I.; Elguero, J.; Molins, E. *J. Chem. Phys.* **2002**, *117*, 5529.

(59) (a) Politzer, P.; Murray, J. S.; Peralta-Inga, Z. *Int. J. Quantum Chem.* **2001**, *85*, 676. (b) Sukumar, N.; Breneman, C. M. in ref 6c, pp 473−498.

(60) (a) Spackman, M. A.; Byrom, P. G. *Chem. Phys. Lett.* **1997**, *267*, 215. (b) McKinnon, J. J.; Mitchell, A. S.; Spackman, M. A. *Chem. Eur. J.* **1998**, *4*, 2136. (c) McKinnon, J. J.; Mitchell, A. S.; Spackman, M. A. *Acta Crystallogr., Sect. B* **2004**, *60*, 627. (d) Spackman, M. A.; McKinnon, J. J.; Jayatilaka, D. *CrystEngComm* **2008**, *10*, 377.

(61) Hirshfeld, F. L. *Theor. Chim. Acta* **1977**, *44*, 129.

(62) Bader, R. F. W.; Gatti, C. *Chem. Phys. Lett.* **1998**, *287*, 233.

(63) (a) Gatti, C.; Cargnoni, F.; Bertini, L. *J. Comput. Chem.* **2003**, *24*, 422. (b) Overgaard, J.; Schiott, B.; Larsen, F. K.; Iversen, B. B. *Chem. Eur. J.* **2001**, *7*, 3756.

(64) Gatti, C.; Lasi, D. *Farday Discuss.* **2007**, *135*, 55.

(65) These errors arise from the errors in the integration procedures, which may be related to the magnitude of the integrated Laplacian, which should in principle be zero because of the conditions of the zero-flux surface[66] but may be as large as $\sim 10^{-3}$ e Å^{-5}. One computationally very demanding method of tackling this problem has been proposed by Gatti and Lasi.[64]

(66) Bader, R. F. W. *Theor. Chem. Acc.* **2001**, *105*, 276.

(67) Holladay, A.; Leung, P.; Coppens, P. *Acta Crystallogr., Sect. A* **1983**, *39*, 377.

(68) The d-orbital description is dependent on the local coordinate system used to define the multipoles on the Cu(II) centers. An identical coordinate system was used for all complexes, with the *x*-direction defined along the Cu(1)−O(1) bond and the *y*-direction along the Cu(1)−N(1) bond. See Sabino, J. R.; Coppens, P. *Acta Crystallogr., Sect. A* **2003**, *59*, 127.

(69) Wiberg, K. B.; Rablen, P. R. *J. Comput. Chem.* **1993**, *14*, 1504.

(70) Bader, R. F. W.; Matta, C. F. *J. Phys. Chem. A* **2004**, *108*, 8385.

(71) (a) Scherer, W.; Sirsch, P.; Shorokhov, D.; Tafipolsky, M. ; McGrady, G. S.; Gullo, E. *Chem. Eur. J.* **2003**, *9*, 6057–6070. (b) Tofipolsky, M.; Scherer, W.; Öfele, K.; Artus, G.; Pedersen, B.; Herrmann, W. A.; McGrady, G. S. *J. Am. Chem. Soc.* **2002**, *124*, 5865–5880. (c) Scherer, W.; McGrady, G. S. *Angew. Chem., Int. Ed.* **2004**, *43*, 1782–1806. (d) Scherer, W.; Eickerling, G.; Shorokhov, D.; Gullo, E.; McGrady, G. S.; Sirsch, P. *New. J. Chem.* **2006**, *30*, 309–312. (e) McGrady, G. S.; Haaland, A.; Verne, H. P.; Volden, H. V.; Downs, A. J.; Shorokhov, D.; Eickerling,

G.; Scherer, W. *Chem. Eur. J.* **2005**, *11*, 4921–4934. (f) Scherer, W.; Tafipolsky, M.; Öfele, K. *Inorg. Chim. Acta* **2007**, *361*, 513–520. (g) Resinger, A.; Trapp, N.; Krossing, I.; Altmannshofer, S.; Herz, V.; Presnitz, M.; Scherer, W. *Angew. Chem., Int. Ed.* **2007**, *46*, 8295–8298. (h) Hebben, N.; Himmel, H.-J.; Eickerling, G.; Herrmann, C.; Reiher, M.; Herz, V.; Presnitz, M.; Scherer, W. *Chem. Eur. J.* **2007**, *13*, 10078–10087.

(72) (a) MacDougall, P. J.; Hall, M. B. *Trans. Am. Cryst. Assoc.* **1990**, *26*, 105. (b) Farrugia, L. J.; Evans, C. *C. R. Chim.* **2005**, *8*, 1556. (c) Abramov, Y. A.; Brammer, L.; Klooster, W. T.; Bullock, R. M. *Inorg. Chem.* **1998**, *37*, 6317. (d) Farrugia, L.; Mallinson, P. R.; Stewart, B. *Acta Crystallogr. Sect B* **2003**, *59*, 234. (e) Lee, J.-J.; Lee, G. H.; Wang, Y. *Chem. Eur. J.* **2002**, *8*, 1821.

(73) Farrugia, L. J.; Evans, C. *J. Phys. Chem. A* **2005**, *109*, 8834.

(74) (a) Ruiz, E.; Llunell, M.; Alemany, P. *J. Solid State Chem.* **2003**, *176*, 400. (b) Moreira.I. de, P. R.; Illas, F.; Martin, R. L. *Phys. Rev. B* **2002**, *65*, 155102. (c) Feng, X.; Harrison, N. M. *Phys. Rev. B* **2004**, *70*, 92402. (d) Mackrodt, W. C.; Middlemiss, D. S.; Owens, T. G. *Phys. Rev. B* **2004**, *69*, 115119. (e) Corà, F.; Alfredsson, M.; Mallia, G.; Middlemiss, D. S.; Mackrodt, W. C.; Dovesi, R.; Orlando, R. *Struct. Bonding (Berlin)* **2004**, *113*, 171. (f) Moreira, I. de P. R.; Illas, F. *Phys. Chem. Chem. Phys.* **2006**, *8*, 1645.

(75) (a) Cirera, J.; Alemany, P.; Alvarez, S. *Chem. Eur. J.* **2004**, *10*, 190. (b) Cirera, J.; Ruiz, E.; Alvarez, S. *Inorg. Chem.* **2008**, *47*, 2871.

(76) (a) Pinsky, M.; Avnir, D. *Inorg. Chem.* **1998**, *37*, 5575. (b) Llunell, M.; Casanova, D.; Cirera, J.; Bofill, J. M.; Alemany, P.; Alvarez, S.; Pinsky, M.; Avnir, D. *SHAPE v1.1b* Barcelona, 2005.

(77) (a) Cano, J.; Ruiz, E.; Alvarez, S.; Verdaguer, M. *Comments Inorg. Chem.* **1998**, *20*, 27. (b) Ruiz, E.; Cirera, J.; Alvarez, S. *Coord. Chem. Rev.* **2005**, *249*, 2649.

(78) (a) Gillon, B. *Mol. Cryst. Liq. Cryst.* **1999**, *335*, 53. (b) Gillon, M. In *Magnetism: Molecules to Materials*; Miller, J. S., Drillon, M., Eds.; Wiley-VCHL New York, 2001; Vol. 1. (c) Schweizer, P. *Physica B.* **1997**, *234−236*, 772.

(79) Figgis, B. N.; Mason., R.; Smith, A. R. P.; Varghese, J. N.; Williams, G. A. *J. Chem. Soc., Dalton Trans.* **1983**, 703.

(80) (a) Aebersold, M. A.; Gillon, B.; Plantevin, O.; Pardi, L.; Kahn, O.; Bergerat, P.; von Seggern, I.; Tuczek, F.; Öhrström, L.; Grand, A.; Levièvre-Berna, E. *J. Am. Chem. Soc.* **1998**, *120*, 5238. (b) Aronica, C.; Jeanneau, E.; El Moll, H.; Luneau, D.; Gillon, B.; Goujon, A.; Cousson, A.; Carvajal, M. A.; Robert, V. *Chem. Eur. J.* **2007**, *13*, 3666. (c) Gillon, B.; Cavata, C.; Schweiss, P.; Journaux, Y.; Kahn, O.; Schneider, D. *J. Am. Chem. Soc.* **1989**, *111*, 7124. (d) Baron, V.; Gillon, B.; Plantevin, O.; Cousson, A.; Mathonière, C.; Kahn, O.; Grand, A.; Öhrström, L.; Delley, B. *J. Am. Chem. Soc.* **1996**, *118*, 11822. (e) Baron, V.; Gillon, B.; Cousson, A.; Mathonière, C.; Kahn, O.; Grand, A.; Öhrström, L.; Delley, B.; Bonnet, M.; Boucherle, J.-X. *J. Am. Chem. Soc.* **1997**, *118*, 3500.

JP804865J